

STUDY OF HYDROGEN RISK IN A MARINE NUCLEAR REACTOR DURING A  
LOSS OF COOLANT ACCIDENT

A Thesis

by

GUILHERME TRINDADE VILELA

Submitted to the Graduate and Professional School of  
Texas A&M University  
in partial fulfillment of the requirements for the degree of

MASTER OF SCIENCE

Chair of Committee,	Yassin A. Hassan
Committee Members,	Maria King
	Rodolfo Vaghetto
Head of Department,	Michael Nastasi

August 2023

Major Subject: Nuclear Engineering

Copyright 2023 Guilherme Trindade Vilela

## ABSTRACT

Marine nuclear reactors, especially when powering submarines, take most of the benefits which this technology can provide. Due to their high power density, small fuel storage volume required, and the long or even dismissed interval of refueling, marine reactors provide good applicability of nuclear technology. However, the cladding of the reactor fuel elements employs materials that can generate hydrogen posing combustion risks and threats to the containment integrity. Space is limited in a marine reactor containment, and a small amount of hydrogen released can become a potential combustion source. In this study, a computational simulation using the commercial multi-purpose code ANSYS Fluent was performed to provide local distributions of temperature, pressure, hydrogen, and steam concentrations in a reactor containment. These parameters were used for the assessment of hydrogen combustion risk during an accidental scenario. The utilization of a multipurpose code presented the inconvenience of the absence of in-built phase change models for condensation modeling. The condensation phenomenon was modeled in the code through the implementation of external subroutines to introduce steam mass sinks and water mass sources on the domain cells. The magnitude of these sources was calculated based on empirical condensation correlations. During the progression of an accident, condensation plays an important role in limiting pressure increase and increasing heat removal in the containment structures. Moreover, condensation also affects the hydrogen combustion risk as it reduces the volume fraction of steam in the containment atmosphere and allows the expansion of the flammable

hydrogen cloud. Hydrogen combustion risk and the possibility of slow deflagration, flame acceleration, and deflagration to detonation transition were assessed from the utilization of the Sigma and Lambda criteria. A theoretical zero-dimensional model has been proposed for the validation of the simulation results, due to the absence of experimental data.

## DEDICATION

*This thesis is dedicated to God,  
my parents, Luiz and Maria de Jesus,  
my sister, Luíza,  
and my wife, Amanda.*

## ACKNOWLEDGMENTS

I would like to thank my committee chair, Prof. Yassin Hassan, and my committee members, Prof. Rodolfo Vaghetto, and Prof. Maria King, for their contribution to this thesis. I would also like to thank Prof. Kevin Fernández for his guidance and support throughout this research.

Thanks also go to my friends and colleagues from the Nuclear Engineering Department and the Thermal-Hydraulics Research Laboratory, Marcos, Esteban, Lee, Thabit, Joanne, Freddy, Faisal, David, and August, for making my time at Texas A&M University a great experience.

I would like to acknowledge the importance and thank my parents, Luiz and Maria de Jesus, and my sister, Luíza, for all the love I received all my life, which made this accomplishment possible. Finally, thank you, Amanda, for joining me on this adventure in Aggieland. Your love and daily support not only made me go farther, but also made my journey lighter and full of joy. I am very lucky to have you in my life.

## CONTRIBUTORS AND FUNDING SOURCES

This work was supervised by a thesis dissertation committee consisting of Professor Yassin Hassan and Professor Rodolfo Vaghetto, from the Department of Nuclear Engineering and Professor Dr. Maria King of the Department of Biological and Agricultural Engineering. Additional contributions and weekly follow-ups were provided by Dr. Mikel Fernández, Visiting Professor at Texas A&M University. Technical orientation and guidance were provided by the Brazilian Navy Captain Osmar Conceição.

Graduate study was supported by a fellowship from the Brazilian Navy. Its contents are solely the responsibility of the author and do not necessarily represent the official views of the sponsor.

## NOMENCLATURE

### Acronyms

ASME	American Society of Mechanical Engineers
CFD	Computational fluid dynamics
DBLM	Diffusive Boundary Layer Model
DDT	Deflagration to Detonation Transition
FA	Flame Acceleration
HMTA	Heat and Mass Transfer Analogy
KWU	Kraftwerk Union
LOCA	Loss of coolant accident
NC	Natural Convection
NCG	Non-condensable gases
NRC	Nuclear Regulatory Commission
NUPEC	Nuclear Power Engineering Center
PP	Primary Pump
PWR	Pressurized Water Reactor
RPV	Reactor Pressure Vessel
SD	Slow Deflagration
THAI	Thermal-hydraulics, Hydrogen, Aerosols, and Iodine Project
US	United States of America

## General notation

$A$	: area
$c_p$	: specific heat at constant pressure
$c_v$	: specific heat at constant volume
$D$	: mass diffusion coefficient
$E$	: energy
$g$	: gravity acceleration
$h$	: heat transfer coefficient, specific enthalpy
$\bar{h}$	: average heat transfer coefficient
$\bar{h}_L$	: average heat transfer coefficient with respect to wall length
$h_{fg}$	: specific latent heat
$h'_{fg}$	: modified specific latent heat
$i$	: index
$k$	: thermal conductivity
$L$	: characteristic length
$L_e$	: room characteristic size
$m$	: mass
$m'''$	: volumetric mass source rate
$M$	: molar mass
$n$	: mole number
$\dot{m}_c$	: condensation mass rate
$P$	: pressure

$q$  : heat transfer rate  
 $q''$  : heat flux  
 $q'''$  : volumetric heat rate  
 $Q$  : heat  
 $R$  : gas constant  
 $T$  : temperature  
 $U$  : internal energy  
 $u$  : specific internal energy  
 $V$  : volume  
 $X$  : mole fraction  
 $W$  : weight fraction, work

#### Greek letters

$\rho$  : mass density  
 $\mu$  : dynamic viscosity  
 $\nu$  : kinematic viscosity  
 $\phi$  : gas species stoichiometric ratio  
 $\sigma$  : expansion rate  
 $\lambda$  : DDT parameter

#### Subscripts

$a$  : activation, air  
 $b$  : bulk, burnt

$c$  : condensation, containment  
 $f$  : fluid  
 $i$  : interface  
 $in$  : inlets  
 $l$  : liquid water, lean mixture  
 $nc$  : non-condensable, natural convection  
 $out$  : outlets  
 $r$  : rich mixture  
 $sat$  : saturation  
 $st$  : steam  
 $st, v$  : steam in the gas phase  
 $u$  : unburnt  
 $v$  : vapor steam  
 $w$  : wall  
 $1$  : state 1  
 $2$  : state 2  
 $1 \rightarrow 2$  : from state 1 to state 2

#### Non-dimensional groups

$Re_\delta$  : Reynolds number with respect to film thickness

$Pr$  : Prandtl number

## Superscripts

\* : critical

*i* : species *i*

## TABLE OF CONTENTS

	Page
ABSTRACT .....	ii
DEDICATION .....	iv
ACKNOWLEDGMENTS.....	v
CONTRIBUTORS AND FUNDING SOURCES.....	vi
NOMENCLATURE.....	vii
TABLE OF CONTENTS .....	xii
LIST OF FIGURES.....	xiv
LIST OF TABLES .....	xvii
1. INTRODUCTION.....	1
1.1. Previous studies.....	4
2. CONDENSATION.....	8
2.1. Pure steam condensation .....	9
2.2. Steam condensation in the presence of non-condensable gases.....	11
2.2.1. Theoretical models based on conservation equations .....	12
2.2.2. Theoretical models based on the heat and mass transfer analogy .....	13
2.2.3. Empirical models.....	13
3. HYDROGEN .....	21
3.1. Hydrogen Flammability .....	23
3.1.1. Slow deflagration .....	24
3.1.2. Flame acceleration.....	26
3.1.3. Deflagration to detonation transition.....	28
4. MODELS AND METHODS .....	31
4.1. Description of the problem.....	31
4.2. Theoretical zero-dimensional model.....	34

4.2.1. Description of the model .....	34
4.2.2. Application of the model .....	39
4.3. CFD model .....	41
4.3.1. Introduction .....	41
4.3.2. ANSYS Fluent capabilities and limitations.....	43
4.3.3. Geometry modelling and Meshing .....	46
4.3.4. Initial Conditions .....	49
4.3.5. Boundary Conditions.....	49
4.3.6. Bulk Condensation Model.....	51
4.3.7. Wall Condensation Models .....	52
4.4. Definition of scenarios .....	54
5. RESULTS.....	57
5.1. Comparison against zero-dimensional model .....	57
5.2. Grid convergence analysis .....	61
5.3. Comparison of condensation correlations .....	66
5.4. Effect of bulk condensation and evaporation.....	68
5.5. Effect of wall and initial temperatures .....	72
5.6. Effect of the position of the leak .....	75
5.7. Numerical Analysis .....	77
5.7.1. Under-relaxation factors for condensation mass sources .....	77
5.7.2. Residuals .....	78
5.7.3. Condensation/evaporation relaxation coefficients .....	80
5.8. Accident progression.....	81
5.8.1. Steam release.....	81
5.8.2. Hydrogen release.....	82
5.8.3. Hydrogen stratification.....	85
6. CONCLUSION .....	87
REFERENCES.....	90

## LIST OF FIGURES

	Page
Figure 1 – Dehbi’s experimental facility. Reprinted with permission from [25].....	16
Figure 2 – Kataoka’s experimental facility. Reprinted with permission from [26] .....	17
Figure 3 – Empirical HTC for condensation in the presence of NCG .....	19
Figure 4 – Shapiro flammability diagram at 1 atm and 25 °C. Reprinted from [30] .....	23
Figure 5 - Hydrogen and steam release rate. Reprinted with permission from [13] .....	32
Figure 6 - Marine nuclear reactor containment. Reprinted with permission from [13] ...	33
Figure 7 – Control volume, initial and boundary conditions for validation model.....	34
Figure 8 – Specific internal energies of saturated steam and liquid.....	37
Figure 9 – Mass of liquid transient obtained from the zero-dimensional model .....	40
Figure 10 – Temperature transient obtained from the zero-dimensional model .....	41
Figure 11 – Pressure transient obtained from the zero-dimensional model .....	41
Figure 12 – Modelled geometry .....	47
Figure 13 – Base mesh (element size 0.5 m).....	48
Figure 14 – Wall layer mesh (gray) .....	49
Figure 15 – Natural convection heat transfer coefficients .....	51
Figure 16 – Temperature transient from E1, S1, E2, and S2 .....	58
Figure 17 – Liquid mass transient from E1, S1, E2, and S2 .....	58
Figure 18 – Pressure transient from E1, S1, E2, and S2 .....	59
Figure 19 – Meshes M3 (0.5 m) and M2 (0.25 m).....	62
Figure 20 – Mesh M1 (0.125 m) .....	62
Figure 21 – Pressure transient from S3, S4, and S5 .....	64
Figure 22 – Temperature transient from S3, S4, and S5 .....	65

Figure 23 – Water liquid mass transient in the containment from S3, S4, and S5.....	65
Figure 24 – Temperature and liquid mass transient from S6, S7, S8.....	67
Figure 25 – Fraction of the containment under SD and FA risk from S6, S7, S8.....	67
Figure 26 – Average DDT index in the main cabin from S6, S7, S8.....	67
Figure 27 – Temperature and liquid mass transient from S9, S10, S11.....	69
Figure 28 – Temperature and liquid mass transient from S6 and S9 .....	70
Figure 29 – Condensation rate and Average steam mole fraction from S6 and S9 .....	70
Figure 30 – Fraction of the containment under SD and FA risk from S6 and S9.....	70
Figure 31 – Average DDT index in the main cabin from S6 and S9 .....	71
Figure 32 – Temperature and liquid mass transient from S7, S12, and S13 .....	72
Figure 33 – Condensation rate and average steam fraction from S7, S12, and S13 .....	72
Figure 34 – Fraction of the containment under SD and FA risk from S7, S12, and S13.....	73
Figure 35 – Average DDT index in the main cabin from S7, S12, and S13 .....	73
Figure 36 – Temperature and liquid mass transient from S7, S14, and S15.....	74
Figure 37 – Condensation rate and average steam fraction from S7, S14, and S15 .....	74
Figure 38 – Fraction of the containment under SD and FA risk from S7, S14, and S15.....	74
Figure 39 – Positioning of the breaks in the primary circuit for S6 and S17 .....	75
Figure 40 – Temperature and liquid mass transient from S6 and S17 .....	76
Figure 41 – Fraction of the containment under SD and FA risk from S6 and S17 .....	76
Figure 42 – Average DDT index in the main and auxiliary cabin from S6 and S17 .....	76
Figure 43 – Temperature and liquid mass transient from S18, S19, and S20.....	77
Figure 44 – Fraction of the containment under SD and FA risk from S18, S19, S20.....	77
Figure 45 – Iterations required per time step and residuals for S18, S19, and S20 .....	78
Figure 46 – Temperature and condensation rate transient from S18 and S21 .....	78

Figure 47 – Iterations required per time step and residuals from S18 and S21 .....	79
Figure 48 – Mass imbalance and liquid mass from S18 and S21 .....	79
Figure 49 – Temperature and liquid mass transient from S18, S22, and S23 .....	80
Figure 50 – Condensation and evaporation mass rates from S18, S22, and S23 .....	80
Figure 51 – Fraction of the containment under SD and FA risk from S18, S22, S23.....	81
Figure 52 – Steam mole fraction in the break longitudinal plane at 340 and 1500 sec ....	82
Figure 53 – Temperature and hydrogen profile at cabin longitudinal section, 2810 sec ..	83
Figure 54 – Containment zones under SD and FA risk at 2300 sec.....	84
Figure 55 – Containment zones under SD and FA risk at 2370 sec.....	84
Figure 56 – Containment zones under SD risk at 2505 sec .....	84
Figure 57 – Containment zones under SD risk at 3060 sec .....	85
Figure 58 – Average temperature and hydrogen mole fraction transient.....	85
Figure 59 – Hydrogen and steam mole fraction on the longitudinal plane at 3100 sec ...	86
Figure 60 – Hydrogen mole fraction on the longitudinal plane at 3400 and 5000 sec ....	86

## LIST OF TABLES

	Page
Table 1 : Containment hydrogen risk analysis available in academic literature .....	7
Table 2 : Typical values of the convection heat transfer coefficient.....	8
Table 3 : Summary of condensation correlations and range of applicability .....	18
Table 4 : Thermodynamic properties of gas species at 25°C and 100 kPa .....	21
Table 5 : Properties of the mixture for DDT criteria.....	29
Table 6 : Constants for DDT criteria.....	30
Table 7 : Dimensions of devices in a marine nuclear reactor containment.....	33
Table 8 : Model inputs .....	39
Table 9 : Summary of estimations by the zero-dimensional model .....	40
Table 10 : Summary of simulations performed by the CFD model .....	56
Table 11 : Comparison between zero-dimensional and CFD models (E1 and S1).....	59
Table 12 : Comparison between zero-dimensional and CFD models (E2 and S2).....	59
Table 13 : Characteristics of meshes employed .....	62
Table 14 : Summary of simulations for grid convergence analysis .....	66
Table 15 : Summary of simulations for comparison of condensation correlations.....	68
Table 16 : Summary of simulations for comparison of influence of bulk phase change .	71
Table 17 : Summary of simulations for assessment of the effect of wall temperature ....	73
Table 18 : Fractions of the containment under SD and FA risk (S6).....	83

## 1. INTRODUCTION

Nuclear power provides flexibility and dispatchability to the energy matrix and is a suitable option to integrate the low-carbon energy system to meet the environmental agreements established [1]. Besides the discussion about low-emission energy sources, there are some applications that must take advantage of the benefits provided by nuclear technology. During the operations realized in Afghanistan and Iraq, US military forces identified weaknesses that came from power supply vulnerabilities and high operating costs as a result of petroleum dependence. Also, due to operational issues and fuel availability necessities, nuclear reactors are suitable for satellites and spacecraft applications [2].

In particular, nuclear technology has found significant applicability in powering submarines in replacement of conventional diesel-electric propulsion. The utilization of nuclear fission as the heat source for the power cycle perfectly suits the tactical requirements of navy warships. Nuclear-powered submarines have eliminated air dependency, since combustion has been replaced by nuclear fission to generate the steam required by the turbines, and thus, a significant tactical advantage is obtained by the increase in the concealment capacity of the submarine. Furthermore, due to its higher power density, larger velocities can be achieved, and no replenishment operation is required [3]. All these factors provide such a substantial increase in the nuclear-powered submarine capacity in comparison to conventional diesel-electric propulsion, that the

tactical benefits can largely support the safety drawbacks associated with the utilization of radioactive material as fuel.

In this regard, redundant and diverse safety systems are required to be designed for a nuclear plant to ensure its safe operation. The design process of safety systems must be guided by a conservative approach and is ruled by regulatory requirements from governmental regulatory agencies. In the United States, the US Nuclear Regulatory Commission (NRC) establishes guidance and technical requirements expressed in Part 50 of Title 10 of the Code of Federal Regulations [4].

This work particularly aims to address the problem of a loss of coolant accident (LOCA) in a marine nuclear reactor regarding the combustion risk due to the release of flammable gases from the uncooled reactor. As a result of the specificities of a marine nuclear reactor design, in which space is a severe limitation, the reactor containment shall not rely on large dry volumes to overcome such large releases of superheated steam. Therefore, without much free volume for steam expansion, a high overpressure can be expected. Nevertheless, this safety concern can be addressed by the containment design, and values up to 5 bars can be withstood without compromising the shielding function [5].

On the other hand, the hydrogen production by the zirconium present in the fuel element cladding is a safety concern as it has been demonstrated by accidents over the last decades [6]. In summary, if a nuclear reactor loses its cooling capability by means of a break in the coolant pipes, it will shut down, but residual heat would continue to be released by the fuel and after a short amount of time, the increase in the fuel element temperature would catalyze an oxidation reaction between oxygen and zirconium present

in the fuel cladding. This reaction releases a large amount of hydrogen and heat into the containment.

Even though a limited amount of hydrogen is released in comparison to the amount of pressurized coolant water that flashes and evaporates when it is released to the lower pressure of the containment, the flammability of this gas brings serious concerns, and it is more likely to compromise the shielding function of the containment structure than the overpressurization from the steam released.

The combustion occurrence and the flame propagation regimes are known to be a result of the properties of the flammable mixture of air and hydrogen, and they are also affected by thermodynamic conditions [7]. Therefore, in order to provide an assessment of the combustion risk, the transport of hydrogen in the containment must be investigated. Moreover, the presence and dynamics of the other gaseous species in the containment must be accounted for.

Steam condensation is a phase change mechanism with several implications for Nuclear Safety, and thus, it will receive special attention and will be focused on throughout this thesis. Up to some point, its occurrence is desired as it limits the pressure increase in the containment and enhances heat transfer in the walls, removing the residual heat that cannot be effectively cooled after the loss of coolant. Nevertheless, steam condensation reduces the fraction of steam in the gaseous mixture, which increases the hydrogen concentration and increases the flammability of the mixture. Therefore, this thesis is dedicated to investigating the hydrogen combustion risk in the containment of a marine nuclear reactor during a LOCA.

Condensation is expected to play an even more relevant role in the transient of an accident scenario of a marine nuclear reactor, as a consequence of the external areas adjacent to the containment being at lower temperatures than regular land power plants. Therefore, as an outcome of this study, an assessment of the influence of condensation models on hydrogen risk shall be performed.

### **1.1. Previous studies**

Hydrogen generation is a significant concern in nuclear reactor safety, and the considerably recent accidental episodes brought the topic back into the discussion. Moreover, the improvement of computational tools for the simulation of transient accidental scenarios has allowed and enhanced nuclear safety analysis. A significant amount of work has been performed concerning assessment of combustion risk and mitigation of its consequences in nuclear facilities.

Valdepeñas (2007) has investigated the hydrogen combustion regimes in two PWR containments (Westinghouse and Siemens KWU) using the CFD code Ansys Fluent [8]. Even though this work was performed almost two decades ago, when fewer tools were available and computational processing capacity was lower, many physical phenomena were accounted for such as steam condensation on the walls in the presence of non-condensable gases, heat conduction, fog, and bulk condensation. By validating his models against the experimental test facilities MISTRA and NUPEC, with regard to steam condensation and gaseous species diffusion, Valdepeñas consolidated an accurate model able to account for the main mechanisms affecting hydrogen risk and using a multi-purpose commercial CFD code.

Prabhudharwadkara (2010) also used a CFD code to assess the concentration of hydrogen in a typical Indian Nuclear Reactor [9] for different conditions of hydrogen release in a containment of 41,000 m<sup>3</sup>. In this study, the presence of steam was not simulated, since it aimed to predict the locations of higher hydrogen concentration. By using this simplification, a long transient simulation became feasible and the turbulence model standard k- $\epsilon$  was verified to accurately and economically predict hydrogen mixing.

Visser (2012) validated a CFD model and simulated the hydrogen and steam release from the HM-2 test performed in the German THAI facility. He used the multi-purpose Ansys Fluent CFD code, in which additional functions beyond the capabilities of the code such as wall condensation were implemented. The chosen facility was a test facility and had a volume of 60m<sup>3</sup>, which is considerably smaller than typical reactor containments. This allowed the study to employ cells as refined as 15 mm at the walls and it added up to 2.5 million cells in the mesh. Comparing simulations results against experimental data, he assessed the influence of turbulence models, wall treatment, and mesh resolution on the suitable modeling of the transient [10].

More recently, Raman (2022) studied the hydrogen distribution in an Indian PWR design [11], previously investigated by Prabhudharwadkara (2010). Raman extended the former analysis by accounting for the steam release and modeling its condensation on the walls through the heat and mass transfer analogy. Raman employed 120,000 cells which were sufficient to model the containment geometry and he reported that ten hours of accident transient took 40 months of processing. He also concluded that steam

condensation substantially affects the other gaseous species distribution in the containment during the accident.

Gharari (2022) investigated the gases distribution inside a WWER1000/V446 containment using Ansys Fluent code [12]. The accidental scenario modeled was a large break LOCA followed by a station blackout. This analysis did not account for steam condensation and it was compared against MELCOR results. Gharari verified the limitations of the simulation due to neglecting steam condensation. The hydrogen concentrations obtained by CFD were up to 2% lower than MELCOR estimations, and pressure peaks 15% higher.

With regard to nuclear reactor accidents with hydrogen release in warships and submarines, a limited number of references were found available in the academic literature due to the strategic and confidential aspects involving military topics. Zhao (2022) investigated the hydrogen risk in a marine nuclear reactor during an accidental scenario [13]. The same containment geometry was investigated by Lyu (2020) for an assessment of the hydrogen control system performance in the same accidental scenario [14]. Both studies were performed using GASFLOW code, and modeled a geometry of about 1000 m<sup>3</sup> with hexahedral cells of 50 cm. No information is found regarding steam condensation modeling.

The studies presented above are summarized in Table 1:

**Table 1 : Containment hydrogen risk analysis available in academic literature**

<b>Reference</b>	<b>Geometry</b>	<b>V (m<sup>3</sup>)</b>	<b>Cell Size (m)</b>	<b>Number of cells</b>	<b>Condensation</b>
Valdepenãs (2007)	Westinghouse and KWU	58,000 and 64,000	Not reported	90,000 and 214,000	Walls and Bulk
Prabhudharwadkara (2010)	Indian PHWR	41,000	0.03~0.5	$1.5 \cdot 10^6$	No
Visser (2012)	THAI HM-2	60	0.02~0.05	$1.75 \cdot 10^5$ - $2.5 \cdot 10^7$	Walls and Bulk
Raman (2022)	Indian PHWR	41,000	0.4	$5.3 \cdot 10^5$	Walls
Gharari (2022)	WWER1000	71,040	0.1~0.9	$6 \cdot 10^5$ ~ $9 \cdot 10^6$	No
Lyu (2020) and Zhao (2022)	Marine reactor	1,000	0.5	8,000	No

## 2. CONDENSATION

Steam condensation phenomenon plays a role of major importance in nuclear safety. From a containment safety analysis perspective, after a postulated accident with steam release from the coolant system, steam condensation occurrence is desired as it limits the containment pressure increase and enhances heat transfer to the walls and structures. Table 2 summarizes typical values of the heat transfer coefficients from convection mechanisms [15]. It can be noticed the substantial heat transfer increase when the phase change occurs:

**Table 2 : Typical values of the convection heat transfer coefficient**

Process	$h$ (W/m <sup>2</sup> K)
Free convection	
Gases	2-25
Liquids	50-1,000
Forced convection	
Gases	25-250
Liquids	100-20,000
Convection with phase change, boiling, or condensation	2,500-100,000

The condensation phenomenon occurs whenever the temperature of a vapor decreases below its saturation temperature, or the partial pressure of the vapor increases above the saturation pressure. After vapor reaches a cool surface, it condenses and releases latent heat from its phase change to the wall. This process, known as surface condensation, can occur in two manners. Initially, drops can be formed on the surface, what is known as dropwise condensation. Although this mechanism is considerably effective for heat transfer to the surface, this condition cannot be maintained permanently, and the formation of a condensate liquid film coalesces the individual droplets on the surface. This

mechanism is known as film condensation and its heat transfer rates are one order or magnitude lower than rates from dropwise condensation [15]. Since this is the dominant condensation mechanism and the most conservative regarding containment heat removal, film condensation received much more attention from researchers, and it will be focused by the literature review throughout this thesis.

Much effort has been made by scholars in order to model steam condensation on surfaces. Generally, the approach found by researchers is to link the effectiveness of this heat transfer mechanism, expressed by the condensation heat transfer coefficient  $\bar{h}$ , to the condensation mass rate,  $\dot{m}$ . This can be done by assuming that the latent heat released from steam condensation is rejected to the wall:

$$\bar{h}A(T_b - T_w) = h_{fg}\dot{m}_c \quad 1$$

The following subsections are dedicated to describing the most relevant correlations that have been proposed. They are grouped as pure steam condensation and condensation in the presence of non-condensable gases. Moreover, these correlations are commonly classified as theoretical, either based on Heat and Mass Transfer Analogy (HMTA) or Diffusive Boundary Layer Model (DBLM), and also empirical.

## **2.1. Pure steam condensation**

The first efforts to obtain a model able to represent the filmwise steam phase change were performed by Nusselt theoretical work in 1917. Nusselt solved the momentum conservation equation in the direction of the surface by adopting some simplifying assumptions such as the existence of pure steam in the condensate-gas interface, laminar flow in the condensate film, constant thermodynamic properties for the

film, steam at the saturation temperature, no heat transfer by conduction from the gas phase to the film and a linear temperature distribution profile in the film. Using the velocity profile obtained for the film, Nusselt proposed the average condensation heat transfer coefficient at the surface for a laminar-regime film:

$$\bar{h}_L = 0.943 \left[ \frac{\rho_f g (\rho_l - \rho_v) h_{fg} k_l^3}{\mu_l L (T_{sat} - T_w)} \right]^{0.25} \quad 2$$

which allows the calculation of the condensation heat flux to the wall and the condensation mass rate at the film surface:

$$q = \bar{h}_L A_w (T_{sat} - T_w) \quad 3$$

$$\dot{m}_c = \frac{q}{h_{fg}} = \frac{\bar{h}_L A_w (T_{sat} - T_w)}{h_{fg}} \quad 4$$

Nusselt and Rohsenow suggested to use a modified steam latent heat to account for thermal advection effects initially neglected:

$$h'_{fg} = h_{fg} + 0.68 c_{p,f} (T_{sat} - T_w) \quad 5$$

Later Kutateladze and Labuntsov proposed condensation heat transfer coefficients for the transition and turbulent-regime film [16]. By assuming that the density of the liquid water is three orders of magnitude higher than steam, the laminar condensation heat transfer coefficient can be simplified as a function of the Reynolds number. These coefficients can be summarized by the following equations:

$$\bar{h}_L = 1.47 Re_\delta^{-\frac{1}{3}} \frac{k_l}{\left(\frac{v_L^2}{g}\right)^{\frac{1}{3}}}, \quad Re_\delta < 30 \quad 6$$

$$\bar{h}_L = \frac{Re_\delta}{1.08Re_\delta^{1.22} - 5.2} \frac{k_l}{\left(\frac{v_l^2}{g}\right)^{\frac{1}{3}}}, \quad 30 < Re_\delta < 1800 \quad 7$$

$$\bar{h}_L = \frac{Re_\delta}{8750 + 58 Pr_l^{-0.5} (Re_\delta^{0.75} - 253)} \frac{k_l}{\left(\frac{v_l^2}{g}\right)^{\frac{1}{3}}}, \quad Re_\delta > 1800 \quad 8$$

The correlation above cannot be applied to the wall heat transfer in practical nuclear containment applications, since the hypothesis of pure steam condensation is far from the real scenario. However, these condensation heat transfer coefficients can be assumed as an upper limit for the ones obtained by the correlations that account for the impairments of the presence of non-condensable gases.

## 2.2. Steam condensation in the presence of non-condensable gases

When the steam from a gaseous mixture of steam and air is in contact with a cooler surface, only the steam species is able to change its phase by condensing, which produces a local increase in the concentration of air that acts as a barrier for steam diffusion. Since steam is prevented from reaching the cooler surface, a decrease in the heat transfer to the wall and a reduction of condensation mass rate is observed. Many factors influence steam condensation in the walls as the thermal resistance of the liquid film, wall temperature, gaseous bulk flow, and the diffusive gas boundary layer adjacent to the wall, but the presence of non-condensable gases, such as air initially present inside the containment, and hydrogen, that is released during a severe accident, is claimed as the most significant condition affecting wall condensation [17]. Empirically, it is verified that an amount of 0.5% of air can reduce the condensation rate by 50% [18].

### **2.2.1. Theoretical models based on conservation equations**

Similar to the theoretical approach followed by Nusselt for pure steam condensation, several authors resorted to the solution of the conservative equations of mass, momentum, and energy at the condensate liquid film and the gaseous boundary layer adjacent to the wall in order to obtain the condensation heat transfer coefficient in the presence of non-condensable gases.

Minkowycz and Sparrow (1966) provided correlations for condensation heat transfer coefficients by solving the boundary layer equations for an isothermal plate under free and laminar forced convective condensation. Along with their solutions, they relied on similarity transformation and worked with stream functions for flow representation. Later, in 1991, Dehbi solved the problem of the turbulent condensation regime by using a similar approach to the similarity transformation used by Minkowycz and Sparrow [19].

Although these theoretical correlations do not rely on experimental results, and thus would not be restricted to a specific range of physical parameters in which they were tested, their implementation in a CFD code is unfeasible as the condensation equations depend on the manner the conservation equations are formulated [17]. Also, the accurate discretization of the boundary layer adjacent to the condensing wall would require a large number of mesh elements, which would not be an option when a geometry as large as a nuclear reactor containment is modeled. For this reason, theoretical models based on conservation equations will not be further described hereafter, nor implemented by the CFD simulations composing this study.

### **2.2.2. Theoretical models based on the heat and mass transfer analogy**

The heat and mass transfer analogy has been used to tackle the condensation modeling problem by several authors, such as Collier, Peterson, and Herranz. Although these are theoretical models, they do not rely on solving all the conservation equations but only simplified equations involving thermodynamic properties that influence condensation [20].

This approach has been used to calculate convection and condensation heat transfer by the hybrid CFD-LP code GASFLOW. Its application is convenient since there is no need to capture the steam concentration gradient on the diffusive boundary layer, and condensation is modeled using the Chilton-Colburn empirical analogy, and the mass transfer coefficient is obtained from the convection heat transfer coefficient [21].

### **2.2.3. Empirical models**

The complexity of condensation theoretical models, which frequently did not propitiate their application in nuclear containment analysis, can be overcome by the use of experimental condensation correlations. These models are conceived to be applied for a limited range of boundary conditions, restrict to the configuration and conditions of the experiment, but due to the absence of additional experimental data, some assumptions are claimed to make their application feasible, such as assuming the flow along a cylindrical external surface of a vertical coolant pipe equivalent to the anticipated one for a vertical plane wall.

The implementation of experimental condensation correlations is usually straightforward. An average condensation heat transfer coefficient over a surface is

expressed in terms of the thermodynamic properties of the gaseous mixture of steam and air along the surface, and this parameter is enough to model the condensation phenomenon during the transient analysis.

### **2.2.3.1. Uchida**

The first known empirical correlation for steam condensation in the presence of non-condensable gases was proposed in 1964 by Uchida [22]. This correlation is based on condensation experiments over a vertical surface of 300 mm. For the determination of the condensation heat transfer coefficient, a steady state was pursued in which the steam heat injected into the system was integrally removed by the condensation over the vertical surface. From the temperature monitoring of the coolant, condensing surface, and gas mixture, heat fluxes were obtained, which allowed the calculation of the condensation coefficients, following the approach presented in Eq. 1. The average condensation heat transfer coefficient was verified to depend only on the fraction of non-condensable gases:

$$h = 380 \cdot \left( \frac{W_{nc}}{1 - W_{nc}} \right)^{-0.7} \quad 9$$

The experiment was conducted with a fixed surface temperature of 322 K, so the model does not address the influence of the surface temperature in the condensation phenomena. Nonetheless, this characteristic of the model provides a substantial conservatism to the correlation, with regard to containment heat removal, when applied to containment walls that shall be cooled and kept at temperatures lower than the experiment.

Uchida's correlation was proposed to be valid under the range of non-condensable mass fraction between 0.09 and 0.93, and the range of total pressure between 1 and 2.87 bar.

#### **2.2.3.2. Tagami**

Tagami (1965) worked on the same facility in which Uchida proposed his correlation, but he used a larger cylindrical vertical surface to propose a condensation correlation that would account not only for the steady regime but for the transient originated from the forced convection present in the initial blowdown of a large break LOCA [23]. With regard to the steady-state regime, Tagami found that condensation was dominated by the influence of non-condensables along the wall, in agreement with Uchida's correlation:

$$h = 11.4 + 284 \cdot \left( \frac{1 - W_{nc}}{W_{nc}} \right) \quad 10$$

Tagami's correlation was developed for a lower range of non-condensables compared to Uchida's results. It is valid for mass fractions of air between 0.38 and 0.83, and used the same surface temperature from Uchida's correlation. Comparing Equations 9 and 10, it can be verified that Tagami's correlation suggests lower heat transfer coefficients, compared to Uchida's model.

#### **2.2.3.3. Dehbi**

Dehbi worked in a cylindrical facility of 5 m of height and 0.45 m of diameter, as depicted in Figure 1, to investigate the influence of non-condensable gases concentration along the external vertical surface of a 3.8cm-diameter coolant pipe [24]. Relying on several thermocouples placed on the coolant, bulk region, and on the walls along the

vertical direction of the cylinder, Dehbi concluded that the length of the wall, the bulk and wall temperatures, and the total pressure play a role in the condensation phenomenon, even though their influence does not overcome the effects from the presence of non-condensables in the mixture.

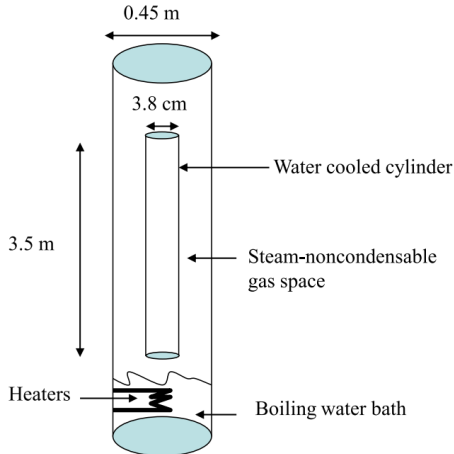


**Figure 1 – Dehbi’s experimental facility. Reprinted with permission from [25]**

This experiment was performed for three different total pressures of 1.5, 3 and 4.5 bar. The mass fraction of non-condensable gases ranged from 0.23 to 0.91 and the wall temperature varied from 10 K to 50 K below the mixture bulk temperature. The flow regime inside the vessel during the different sets of the experiment was turbulent natural convection. Taking advantage of the instrumentation used for the experiment, Dehbi proposed the following correlation for the condensation heat transfer on the surface:

$$h = \frac{L^{0.05}[(3.7 + 28.7P) - (2438 + 458.3P) \cdot \log(W_{nc})]}{(T_b - T_w)^{0.25}} \quad 11$$

#### **2.2.3.4. Kataoka**

Kataoka (1992) performed an experiment to evaluate the heat removal of a passively cooled containment [26]. Kataoka’s experiment relevance can be observed as he

performed the wall condensation investigation in the presence of non-condensables at larger walls (0.4 m x 4.2 m) and verified condensation heat transfer coefficients similar to the ones obtained by Uchida.

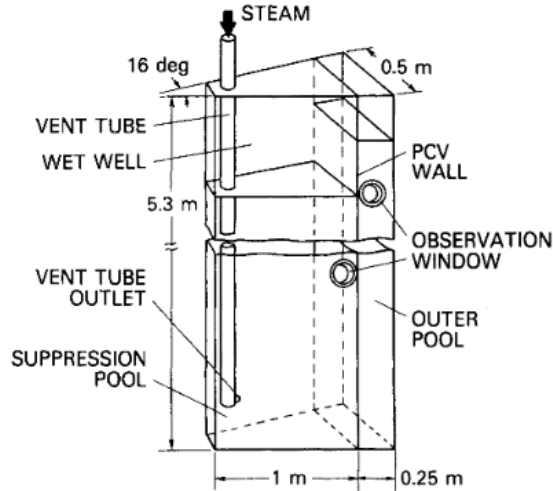


Figure 2 – Kataoka’s experimental facility. Reprinted with permission from [26]

Therefore, the discrepancy between the correlations based on small-scale experiments and the real-size reactor containments in which they were intended to be applied, has decreased. Kataoka presented the experimental results in a correlation very similar to the one proposed by Uchida:

$$h = 430 \cdot \left( \frac{W_{nc}}{1 - W_{nc}} \right)^{-0.8} \quad 12$$

### 2.2.3.5. Summary of experimental correlations

All the correlations selected to be analyzed by this literature review depend strongly on the mass fraction of non-condensable gases ( $W_{nc}$ ), but each one has some specificities and can be also expressed as a function of the wall length ( $L$ ), wall

temperature ( $T_w$ ), gas mixture bulk temperature ( $T_b$ ), and total pressure inside the containment ( $P$ ). These correlations are summarized in Table 3.

**Table 3 : Summary of condensation correlations and range of applicability**

Author	$W_a$	P (bar)	$T_w$ (°C)	$T_b$ (°C)	L (m)
Uchida (1965)	0.09-0.93	1-2.87	49	No data	0.3
Tagami (1965)	0.37-0.83	No data	49	No data	0.9
Dehbi (1991)	0.25-0.9	1.5-4.5	60-110	79-137	0.3-3.5
Kataoka (1992)	0.5-0.9	1-3	30-100	22-110	0.9-4.2
Murase (1993)	0.45-0.97	1-3.5	30-100	22-110	0.9-4.2
Liu (2000)	0.13-0.61	2.5-4.5	100	104-125	2

It is convenient to compare the empirical correlations above presented against maximum theoretical heat transfer coefficients that could limit the condensation heat transfer mechanism on the walls. Resorting to Nusselt's theoretical work, described in Section 2.1, regarding pure steam condensation, the maximum and minimum heat transfer coefficients can be estimated, and compared to the ones obtained from the empirical correlations for condensation in the presence of non-condensable gases. This comparison allows to verify significant reduction in the surface heat transfer mechanism due to the presence of non-condensables. Replacing the liquid water and steam thermodynamic properties in Equations 6, 7 and 8, condensation maximum and minimum heat transfer coefficients are obtained for pure steam condensation, and assumed as reference values for the null weight fraction of non-condensable gases. Figure 3 depicts the maximum and minimum pure steam condensation heat transfer coefficients, and also for mixtures of air and steam, which were plotted using Equations 9, 10, 11, and 12:

### Condensation heat transfer coefficients

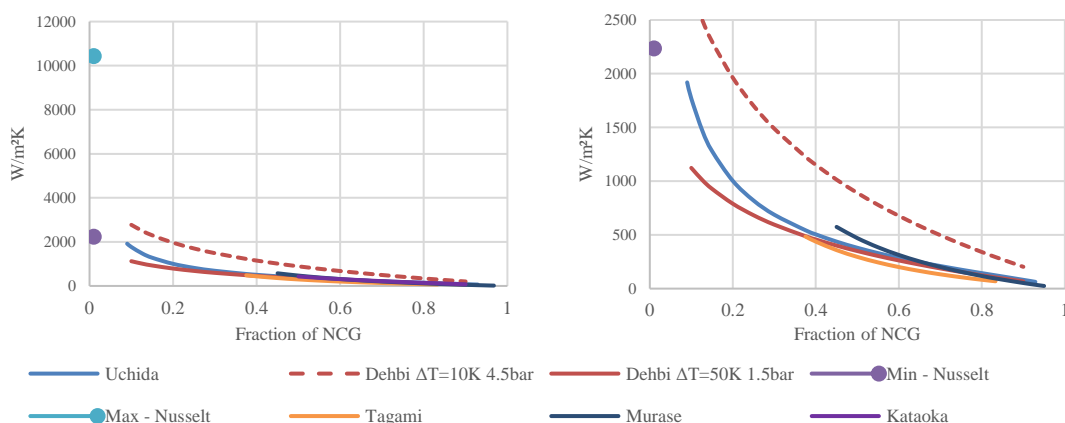


**Figure 3 – Empirical HTC for condensation in the presence of NCG**

Since Dehbi’s correlation is dependent also on additional parameters, its limiting values were plotted for the larger wall length it was proposed. It can be seen that Dehbi’s correlation is able to predict the increase in condensation rates at larger pressures, as it would be expected for the pressures higher than 2 bar, observed in typical post LOCA scenarios [19]. This increase is due to larger driving forces from densities difference [17].

Regardless of the combination of boundary conditions that characterize the condensation phenomenon, Tagami’s correlation provides the lowest heat transfer coefficients.

#### 2.2.3.6. Utilization of condensation correlations in lumped-parameter codes

The choice of the suitable condensation correlation for a transient analysis may affect the results produced and must observe the transient to be analyzed. The boundary conditions of the scenario simulated must match the circumstances under which the experiments were performed since condensation is a phenomenon highly affected by them.

In this context, due to its range of applicability, Uchida’s and Tagami’s correlation have been widely used by safety codes. These experimental correlations are easy to

implement and have been used by GOTHIC, MAAP, COMPACT, CONTEMPT-4 and RELAP [17].

The HMTA theory has also provided the steam mass sinks and liquid sources to model condensation during the progression of an accident in thermal-hydraulics codes as COMMIX-1D, PCCSAC, CONTAIN, CONTEMPT-LT, MELCOR, and TONUS.

### 3. HYDROGEN

During a nuclear severe accident, hydrogen is produced from the oxidation reaction of the zirconium present in the fuel cladding, represented by Equation 13. The oxidation reaction is catalyzed by the temperature increase which becomes uncontrolled when the cladding reaches 1200°C [27], which can easily be achieved when the coolant boils and leaves the fuel element uncovered.



This reaction is an exothermic process that releases significant amounts of energy and hydrogen gas. Both of them provoke undesirable effects in the containment with regard to nuclear safety and require the adoption of mitigation strategies.

From stoichiometric calculations, for each kilogram of zirconium present in the cladding, a maximum mass of 44.2 g of hydrogen can be generated. Also, there is a heat release of 6.5 MJ per kilogram of zirconium through oxidation [6].

Hydrogen is a singular gas species, and when released into the reactor containment, is part of a gaseous mixture in addition to water steam, and air. Table 4 summarizes the thermodynamic properties of species that compose the reactor containment atmosphere during an accident [28]:

**Table 4 : Thermodynamic properties of gas species at 25°C and 100 kPa**

Species	Molar mass (g/mol)	Mass density (kg/m <sup>3</sup> )	Specific heat at constant volume (kJ/kg.K)
Hydrogen	2.02	0.081	10.085
Air	28.97	1.169	0.717
Steam vapor	18.02	0.023	1.410

It can be seen that the produced hydrogen is not only the lighter species but also the one that presents the largest specific heat. Therefore, it can be expected that even lower mass releases can contribute to heating and over-pressurization of the containment. The pressure evolution inside the containment is driven by the mass and temperature of gas species, and the containment pressure can be stated as the sum of the partial pressures of gaseous species in the mixture:

$$P = P_v + P_{H_2} + P_{air} \quad 14$$

Using the ideal gas model:

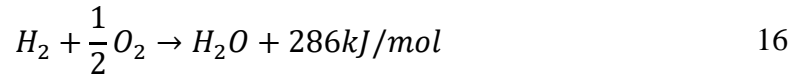
$$P = \frac{RT_c}{V_c} (n_v + n_{H_2} + n_{air}) = \frac{RT_c}{V_c} \left( \frac{m_v}{M_v} + \frac{m_{H_2}}{M_{H_2}} + \frac{m_{air}}{M_{air}} \right) \quad 15$$

Another implication from the lightness (low molar mass) of hydrogen is that even for a low mass release, its contribution to the containment overpressure is significant, as can be understood by Equation 15. Moreover, hydrogen behaves as a non-condensable gas, due to its very low critical point (-240.01 °C and 12.96 bar) [29], during the whole range of thermodynamic transient conditions observed in a nuclear accident, so the condensation phase change mechanism cannot minimize the overpressure as it can occur for steam.

Nonetheless, more dangerous than the overpressure, the hydrogen risk in a nuclear accident is originated by its flammability. After initiating and progressing conditions are met, the flammable mixture of hydrogen and air can reach a detonation and significantly damage the containment structure compromising the shielding function and releasing radionuclides in the atmosphere.

### 3.1. Hydrogen Flammability

Hydrogen is a gas that can react with the oxygen present in the air through a process known as combustion:



The initiating conditions required for the occurrence of combustion are easily found in a nuclear reactor containment during a severe accident. Shapiro and Moffette [30] proposed a diagram gathering experimental data to represent the limits required for the reaction to occur (Figure 4).

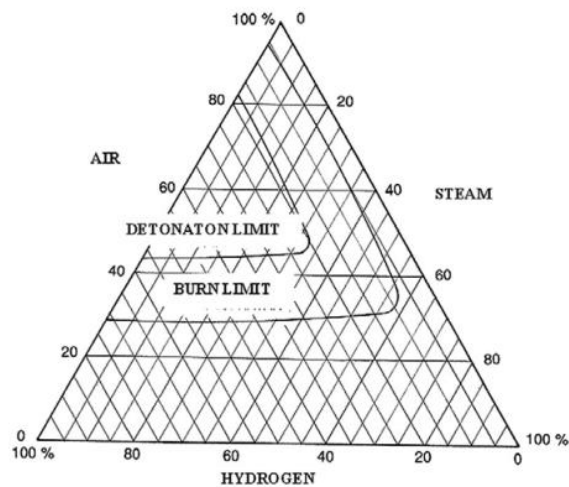


Figure 4 – Shapiro flammability diagram at 1 atm and 25 °C. Reprinted from [30]

Combustion requires a specified range of volume concentration of hydrogen and air, that may vary slightly according to temperature and pressure conditions. Moreover, it also depends on an initiating event known as ignition. In theory, the flammability limits of hydrogen and air could be reached without starting the combustion process. Nonetheless, hydrogen risk assessment does not account for the ignition probability due

to its randomness, rather focusing on gaseous species concentration and thermodynamic properties of the containment atmosphere to assess the hydrogen risk [31].

Combustion researchers have classified combustion according to three main regimes: slow deflagration, flame acceleration and deflagration to detonation transition [32]. Slow deflagration is the transition between an inert gas mixture to a flammable mixture. It is a regime characterized by a flame propagated at a speed lower than the speed of sound and the overpressure produced is about the initial pressure. Flame acceleration is a regime in which the flame velocity is larger than the sound propagating speed on the reactant gases, but lower than the speed of the sound on the burnt products, what is around 500 m/s. For the flame acceleration regime, the overpressure produced can reach ten times the initial pressure. Finally, the deflagration to detonation transition produces flames at speeds higher than sound propagation speed on either the combustion products or reactants, reaching up to 1200 m/s and pressure loads 30 times larger than the initial pressure.

The flame regime is a result of a combination of factors, as hydrogen, air and steam concentrations, the geometry in which the flame propagates, turbulence generation, temperature and pressure of the mixture. Higher hydrogen concentrations lead to higher releases of energy, and thus higher flame velocities.

### **3.1.1. Slow deflagration**

As previously described, combustion occurrence depends mainly on the gases concentration, and it is slightly affected by temperature and pressure variations. Byun [33] initially analyzed experimental results from combustion experiments from Kumar [34],

Stamps and Berman [7] to suggest linear functions that were able to represent the limits between flammable and inert regions. Martín-Valdepeñas improved this analysis and proposed more accurate coefficients to represent the deflagration criteria [35].

Since the experiments reported by Stamps and Berman gather the gaseous mixture temperature, pressure, and species concentrations, with regard to upward and downward flame propagation, the following criteria were proposed:

Lower flammability limit for upwards flame propagation:

$$X_{H_2} \geq 0.037 + 0.011X_v - 0.416 \cdot 10^{-4}(T - 373) \quad 17$$

Lower flammability limit for downwards flame propagation:

$$X_{H_2} \geq 0.086 + 0.008X_v - 1.020 \cdot 10^{-4}(T - 373) \quad 18$$

Upper flammability limit for both propagation directions:

$$X_{H_2} \leq 0.772 - 1.087X_v + 2.71 \cdot 10^{-4}(T - 373) \quad 19$$

$$X_v < 0.63 + 3 \cdot 10^{-4}(T - 373) \quad 20$$

Equations 17 and 18 indicate a negative tendency from the mixture temperature into the lower hydrogen flammability concentration limit. Thus, even lower mole fractions of the flammable gas can combust if the temperature is increased. From the same equations, at 25°C and without any steam present, the lower flammability limits are 4.0% for upward propagation and 9.4% for descending flames. Similarly, Equation 19 shows that higher temperatures can increase the upper flammability limit of hydrogen. At 25 °C and with no steam present, combustion is possible up to 75.2% of hydrogen volume fraction.

Analogously, from the analysis of the equations representing the deflagration criteria with regard to the steam volume fraction, it can be observed that the presence of steam in the gaseous mixture increases the lower flammability limit and decreases the upper one. Additionally, the steam concentration by itself can turn the gas mixture inert as stated by Equation 20.

### **3.1.2. Flame acceleration**

After the occurrence of ignition, the produced flame propagates as a deflagration of a slow laminar air-hydrogen-steam mixture. This flame will preferentially propagate towards the regions with higher hydrogen concentration, dryer mixtures and into regions with higher turbulence generation. Besides the achievement of conditions favorable to the combustion, the self-induced turbulence from the expansion flow of the burned mixture behind the flame may accelerate the flame, thus inducing a transition from slow laminar to fast turbulent deflagration [32].

In order to evaluate the likelihood of the flame acceleration regime after the mixture reaches the deflagration limits described previously, a model proposed by Karlsruhe Research Center and Kurchatov Institute Moscow is applied. This model claims that the flame acceleration is mostly affected by the mixture composition and properties rather than the geometry surrounding the mixture. A parameter called expansion ratio ( $\sigma$ ) should be calculated for each region of the mixture, and compared against a critical value ( $\sigma^*$ ). The expansion ratio corresponds to the ratio of densities of the unburnt and burnt gas mixture, as defined in Equation 21:

$$\sigma = \frac{\rho_u}{\rho_b} \quad 21$$

The calculation of the burned mixture density assumes that the gas mixture suffers an adiabatic and isobaric combustion, so all the heat released by the combustion reaction heats up the mixture. Thus, the densities ratio and temperatures ratio can be obtained by Equation 22.

$$\sigma = \frac{T_b n_b}{T_u n_u} \quad 22$$

It was demonstrated through experiments that this parameter accurately predicts the possibility of a gas mixture to undergo in flame acceleration [36]. The critical expansion rate ( $\sigma^*$ ) can be expressed as a function of unburnt mixture temperature ( $T_u$ ) and activation energy ( $E_a$ ), that also depends on the gas species stoichiometric ratio ( $\phi$ ), as presented in Equations 23, 24 and 25:

$$\sigma^* = 0.9 \cdot 10^{-5} \left(\frac{E_a}{T_u}\right)^3 - 1.9 \cdot 10^{-3} \left(\frac{E_a}{T_u}\right)^2 + 1.807 \cdot 10^{-1} \left(\frac{E_a}{T_u}\right) + 0.2314 \quad 23$$

$$E_a = 7.73 \cdot 10^3 - 4.06 \cdot 10^2 \phi + 8.96 \cdot 10 \phi^2 - 4.32 \cdot 10^{-1} \phi^4 \quad 24$$

$$\phi = \frac{X_{H_2}}{2X_{O_2}} \quad 25$$

Finally, the temperatures and moles quantities in Equation 22 depend on the proportion of reactant species, which can occur in two scenarios according to excess or absence of oxygen to completely combust all the hydrogen. Therefore, gaseous mixtures can be classified as rich or lean. For lean mixtures, all the hydrogen available is burnt, and the expansion rate can be calculated as:

$$\sigma_l = \frac{T_{b,l}}{T_u} \left( 1 - \frac{1}{2} X_{H_2} \right) \quad 26$$

Where the burnt temperature of the lean mixture is calculated as:

$$T_{b,l} = T_u + \frac{n_{H_2} \cdot h_{comb}}{(n_{H_2O} + n_{H_2})c_{p,H_2O} + (n_{O_2} + 0.5n_{H_2})c_{p,O_2} + n_{N_2}c_{p,N_2}} \quad 27$$

For rich mixtures, all the oxygen available reacts, and the expansion rate can be calculated as:

$$\sigma_r = \frac{T_{b,r}}{T_u} (1 - X_{O_2}) \quad 28$$

Where the burnt temperature of the rich mixture is calculated as:

$$T_{b,r} = T_u + \frac{n_{O_2} \cdot h_{comb}}{(n_{H_2O} + 2n_{O_2})c_{p,H_2O} + (n_{H_2} - 2n_{O_2})c_{p,H_2} + n_{N_2}c_{p,N_2}} \quad 29$$

Finally, the flame acceleration is possible if the expansion ratio  $\sigma$ , calculated from Equations 26 and 28, is larger than the critical expansion rate  $\sigma^*$ , obtained by Equation 23. Similarly, the flame acceleration criterion can be summarized by the index  $i_\sigma$ :

$$i_\sigma = \frac{\sigma}{\sigma^*} \quad 30$$

If the index is higher than 1, flame acceleration is possible.

### 3.1.3. Deflagration to detonation transition

Once the flammable mixture undergoes flame acceleration, the transition from the deflagration to detonation regime can occur if some conditions are met, as the mixture composition and the turbulence generation from the propagation of the flame in a confined space. Moreover, the presence of obstacles along the flame path reduces the hydrogen mole fraction necessary to accelerate the flame.

Thus, it was verified that the geometrical characteristics of the flame propagation surroundings must be considered to assess the likelihood of detonation. This parameter is accounted as the room characteristic size ( $L_e$ ), which is a strong simplification for the geometry, even though commonly used, and is calculated from Equation 35:

$$L_e = V^{\frac{1}{3}} \quad 31$$

From experiments performed in different facilities, a parameter based on the flammable mixture properties was fitted by researchers from Kurchatov Institute, which allows the prediction of possibility of deflagration to detonation transition [37]. The proposed parameter is represented by  $\lambda$ , expressed in cm and is calculated from Equation 32:

$$\log(\lambda) = \left[ a - m + \left( b \left( A - \frac{k}{B} \right)^{-f} + h(A - gB)^2 + i(A - gB) \right) \frac{j(1 + dC + eBC^2)}{B} \right] \cdot \left[ (D - c) \left( \frac{1}{0.1 - c} + n(D - 0.1) \right) \right] + m \quad 32$$

Where the variables written in capital letters are properties of the gas mixture, and are summarized Table 5, and the lowercase parameters are constants fitted by the Kurchatov Institute model, and are presented in Table 6:

**Table 5 : Properties of the mixture for DDT criteria**

Variable	Property	Unit
$A$	Dry hydrogen mole fraction	%
$B$	Initial temperature	K
$C$	Steam mole fraction	%
$D$	Initial pressure	MPa

**Table 6 : Constants for DDT criteria**

Variable	Value
<i>a</i>	-1.13331
<i>b</i>	45.9807
<i>c</i>	-0.15765
<i>d</i>	0.0465429
<i>e</i>	$3.5962 \cdot 10^{-7}$
<i>f</i>	0.997468
<i>g</i>	-0.0266646
<i>h</i>	$8.74995 \cdot 10^{-4}$
<i>i</i>	-0.0407641
<i>j</i>	331.162
<i>k</i>	-418.215
<i>m</i>	2.3897
<i>n</i>	-8.42378

The model claims that DDT can occur if the flammable mixture cloud characteristic size ( $L_e$ ) is larger than  $7\lambda$ , what is equivalent to the index  $i_\lambda$  higher than 1, as defined by Equation 33:

$$i_\lambda = \frac{L_e}{7\lambda} > 1 \quad 33$$

## 4. MODELS AND METHODS

### 4.1. Description of the problem

To fulfill the objectives proposed by this thesis, a CFD simulation of the transient of LOCA in a marine nuclear reactor was performed using CFD code ANSYS Fluent 2022 R2. A description of the simulation setup, including geometries, initial and boundary conditions will be presented in the following sections. Moreover, a theoretical model for the assessment of pressure and temperature transients will be proposed in order to preliminarily verify data obtained from the simulation. ANSYS Fluent 2022 R2 capabilities and limitations will also be discussed, as the equations solved by the code and models implemented will be stated.

The particular accident scenario analyzed by this thesis refers to a LOCA in a marine nuclear reactor containment. After the literature review conducted, it was identified two studies which analyzed the hydrogen release in this type of nuclear containment. Zhao (2022) calculated the flame acceleration and the deflagration to detonation transition factors from GASFLOW simulations to assess the hydrogen combustion risk from the LOCA in a marine nuclear reactor cabin of a typical marine pressurized water reactor with a doubled loop [13]. The same accident transient was also studied by Lyu (2020), which focused on the modeling of a hydrogen control system to mitigate combustion risk, also using GASFLOW CFD code [14].

Steam condensation plays a significant role in the accident transient progression. However, there is no description in references [13], [14], about the condensation models

selected for steam phase change. In order to tackle this uncertainty, different condensation models presented previously in the literature review will be considered during the analysis of the transient.

Therefore, to investigate the influence of condensation models on hydrogen combustion risk, the accident transient described by Zhao (2022) and Lyu (2020) will be used as benchmark. For this LOCA in a marine nuclear reactor, the temporal mass release rate of hydrogen and superheated steam is presented in Figure 5:

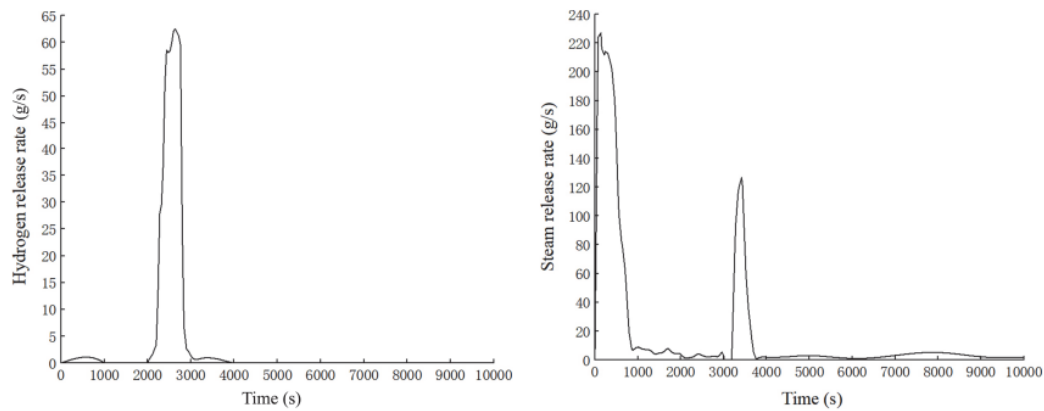


**Figure 5 - Hydrogen and steam release rate. Reprinted with permission from [13]**

The release of steam is concentrated in two main occurrences, and adds up to 150 kg of superheated steam, which evaporates when the pressurized water from the coolant system leaves the primary circuit. Hydrogen release occurs 2193 seconds after the beginning of the accident and totalizes the mass of 30 kg generated from the oxidation of the cladding of the fuel elements. The geometry of the marine reactor containment is significantly smaller than conventional nuclear reactors and is presented in Figure 6.

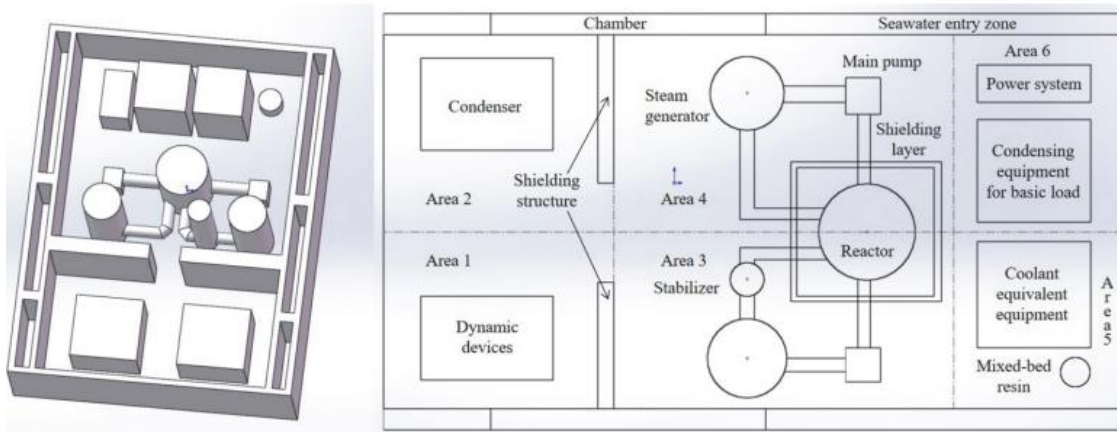


**Figure 6 - Marine nuclear reactor containment. Reprinted with permission from [13]**

The marine nuclear reactor cabin has a hexahedral geometry, its free internal volume is 968.5 m<sup>3</sup>, and its main dimensions are: length of 14 m, width of 10 m, and height of 8 m. Cabin equipment dimensions are detailed in Table 7:

**Table 7 : Dimensions of devices in a marine nuclear reactor containment**

Device	Shape	Key Dimensions (cm)			
		Radius	Length	Width	Height
Core System	Cylinder	150			400
Stabilizer	Cylinder	75			260
Steam generator	Cylinder	65			450
Mixed-bed resin	Cylinder	30			88
Piping	Cylinder	25			
Main Pump	Cuboid		50	50	200
Condenser	Cuboid		200	180	360
Dynamic devices	Cuboid		200	150	360
Power system	Cuboid		200	90	280
Condensing equipment for basic load	Cuboid		200	210	580
Coolant equivalent equipment	Cuboid		200	210	580

## 4.2. Theoretical zero-dimensional model

### 4.2.1. Description of the model

Due to the absence of experimental results for validation of the results obtained by this study, a theoretical approach is proposed by the author, even though substantially simplified. This model relies on mass and energy conservation equations and provides reasonably accurate estimations for pressure and temperature transients.

This model does not carry any detailed geometrical characteristics from the real containment analyzed, and it will be referred to through this thesis as zero-dimensional model. This model only accounts for a generic control volume of volume  $V_c$ , in which two different gas species are injected: superheated steam from the boiled reactor coolant inventory at mass rate  $\dot{m}_v(t)$  and hydrogen gas from the oxidation of the cladding at mass rate  $\dot{m}_h(t)$ . Both releases are assumed to occur at constant temperatures  $T_v$  and  $T_{H_2}$ , for the steam and hydrogen respectively. Figure 7 illustrates the model:

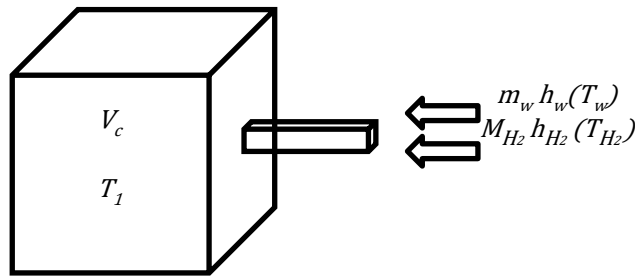


Figure 7 – Control volume, initial and boundary conditions for validation model

The model is based on the energy conservation equation applied to the control volume between states 1 and 2 [28]:

$$U_2 - U_1 = Q_{1 \rightarrow 2} - W_{1 \rightarrow 2} + \sum_i m_{in}^i h_{in}^i - \sum_i m_{out}^i h_{out}^i \quad 34$$

And based on mass conservation equation:

$$m_2 - m_1 = \sum_i m_{in}^i - \sum_i m_{out}^i \quad 35$$

In the previous equations, the index  $i$  stands for the species present and injected in the control volume. State 1 is characterized by the containment at initial pressure  $P_1$  filled exclusively with air at temperature  $T_1$ . Between states 1 and 2, superheated steam at pressure  $P_v$  and  $T_v$ , and hydrogen at pressure  $P_{H_2}$  and  $T_{H_2}$ , are injected in the containment. The heat exchange between the three gaseous species is assumed to be highly effective, and an equilibrium temperature  $T_2$  is reached over all the control volume.

Equation 34 can be rewritten by decomposing the terms referent to states 1 and 2 in terms of the species present in each state. The subscript  $st$  is used for the steam that remains in the gaseous phase, while the subscript  $l$  is used for the liquid phase. The subscript  $a$  is used for air, and the subscript  $H_2$  is used for hydrogen. Internal energies difference  $U_2 - U_1$  can be expressed in terms of specific internal energies and temperatures of the species, as presented in Equation 36:

$$U_2 - U_1 = (U_{a,2} + U_{l,2} + U_{st,2} + U_{H_2,2}) - U_{a,1}$$

$$U_2 - U_1 = m_{a,2}u_{a,2} + m_{l,2}u_{l,2} + m_{st,2}u_{v,2} + m_{H_2,2}u_{H_2,2} - m_{a,1}u_{a,1} \quad 36$$

$$U_2 - U_1 = m_a u_a(T_2) + m_{l,2}u_l(T_2) + m_{st,2}u_v(T_2) + m_{H_2,2}u_{H_2}(T_2) - m_a u_a(T_1)$$

The only source of work performed in the boundary of the control volume is the work required to inject the gases inside the volume, which is present in the enthalpy terms  $h_{in}^i$ . This way, the following simplification is made:

$$W_{1 \rightarrow 2} = 0 \quad 37$$

Replacing Equations 36 and 37 in the first law of thermodynamics applied to the control volume, we obtain:

$$m_a u_a(T_2) + m_{i,2} u_i(T_2) + m_{st,2} u_v(T_2) + m_{H_2,2} u_{H_2}(T_2) - m_a u_a(T_1) = Q_{1 \rightarrow 2} + m_w h_w(T_v) + m_{H_2} h_{H_2}(T_{H_2}) \quad 38$$

From the initial conditions of the model ( $m_a, T_1, P_1$ ), boundary conditions ( $\dot{m}_v(t), \dot{m}_{H_2}(t), T_v, T_{H_2}$ ) and gaseous species intensive properties ( $u_a, u_w, u_{H_2}, h_w, h_{H_2}$ ); the equilibrium temperature  $T_2$  can be calculated if the heat rejected from the control volume between states 1 and 2,  $Q_{1 \rightarrow 2}$ , is known. The control volume is limited by its external walls, that have total surface area  $A_w$ , and exchange heat with their neighborhood by natural convection. Also, some significant amount of heat is removed from the control volume when steam condenses in the walls.

Assuming natural convection heat transfer mechanism on the walls driven by internal and walls temperature difference (using empirical correlations for the average natural convection heat transfer coefficient  $\bar{h}$ ), the heat flux removed through the control volume boundaries by this mechanism can be expressed as:

$$q_{nc} = -\bar{h} A_w (T_b - T_w) \quad 39$$

In the equation above, the bulk temperature  $T_\infty$  corresponds to the internal temperature of the control volume,  $T_w$  is the temperature of the walls, and  $A_w$  is the surface area of the walls on which natural convections occurs.

Also, there is a significant amount of heat removed by steam condensation on the walls. This amount of heat can be obtained from the amount of mass that condenses and the latent heat of condensation of steam in the temperature of the walls:

$$Q_{cond,1\rightarrow2} = -m_{l,2}h_{fg}(T_w) \quad 40$$

Thus, the total heat rejected by the walls can be obtained by accounting for these two parcels:

$$Q_{1\rightarrow2} = -\int_1^2 q_{nc}dt + Q_{cond,1\rightarrow2} \quad 41$$

In order to make Equation 38 analytically solvable, the gaseous species intensive properties must be linked to the temperature at state 2. This can be achieved by assuming constant specific heats  $c_{v,a}$ ,  $c_{v,H_2}$  and  $c_{p,H_2}$  for air and hydrogen, and linearizing the specific internal energy of the saturated liquid water and steam as a function of  $T_2$ . From Figure 8, it can be seen that from the range of temperatures between 300 and 500 K, the specific internal energies of saturated liquid and steam,  $u_l$  and  $u_v$ , observe a linear behavior with regard to the temperature:

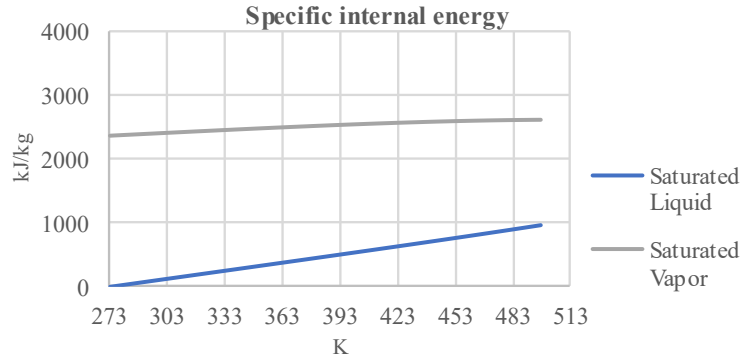


**Figure 8 – Specific internal energies of saturated steam and liquid**

And can be linearized as:

$$u_l(T_2) = K_{1l} + K_{2l}T_2 \quad 42$$

$$u_v(T_2) = K_{1v} + K_{2v}T_2 \quad 43$$

Replacing the linearization expressed by equations above and specific heats for species in Equation 38, and isolating the temperature  $T_2$ :

$$T_2 = \frac{Q_{1 \rightarrow 2} + m_a c_{v,a} T_1 + m_{st,2} h_{st}(T_w) + m_{H_2,2} c_{p,H_2} T_{H_2} - m_{l,2} K_{1l} - m_{st,2} K_{1v}}{m_a c_{v,a} + m_{l,2} K_{2l} + m_{st,2} K_{2v} + m_{H_2,2} c_{v,H_2}} \quad 44$$

The calculation of the final temperature by Equation 44 requires the previous determination of the amount of condensation in the control volume, what will define the mass of each phase of water at the state 2,  $m_{l,2}$  and  $m_{st,2}$ . Since condensation occurs mostly on the walls, where the temperature is lower, this temperature will be accounted for the determination of the saturation temperature of the steam in the control volume. All steam released into the control volume that produces a partial pressure higher than the saturation pressure at  $T_2$  will be assumed to promptly condense. The saturation pressure of steam is calculated from Antoine Equation:

$$\ln(P_{sat}) = A + \frac{B}{T + C} \quad 45$$

In which the coefficients  $A$ ,  $B$ , and  $C$  are obtained from [38], and are respectively 23.1512, -3788.02, and -47.3018; and the wall temperature  $T_w$  shall be used as  $T$ . Once  $P_{sat}$  is defined, it is possible to calculate the maximum amount of steam present in the containment, by using the density of saturated steam at the wall temperature  $T_w$ :

$$\rho_{st,sat} = \frac{P_{sat}}{R_w T_w} \quad 46$$

So, the saturated mass of steam in the control volume can be calculated as:

$$m_{st,sat} = \rho_{st,sat} V_c \quad 47$$

And the mass of liquid in the control volume is either zero, if the steam released during the transient does not produce a partial pressure higher than the saturation pressure, or the difference between the injected steam and saturated mass of steam in the temperature of the wall:

$$m_l = \max(0, m_{st,in} - m_{st,sat}) \quad 48$$

Moreover, the final containment pressure can be expressed as the sum of the partial pressures of the gas species present in the containment:

$$P = P_v + P_{H_2} + P_a \quad 49$$

Assuming the ideal gas model, the partial pressures above can be expressed as a function of the amount of mass of gas and their temperatures (assumed to be in equilibrium). For state 2, the total pressure can be written as:

$$P_2 = \frac{RT_2}{V_c} \left( \frac{m_v}{M_w} + \frac{m_{H_2}}{M_{H_2}} + \frac{m_a}{M_a} \right) \quad 50$$

#### 4.2.2. Application of the model

The zero-dimensional model described in the previous section was applied to the benchmark accident scenario analyzed, as a first estimation for the temperatures and pressure transients expected. The model inputs are presented in Table 8:

**Table 8 : Model inputs**

<b>Model inputs</b>	<b>Value</b>
Steam release mass flow rate	Polynomial
Steam release temperature	600 K
Hydrogen release mass flow rate	Polynomial
Hydrogen release temperature	600 K
Containment free volume	968.5 m <sup>3</sup>
Containment initial temperature	300 K
Containment initial pressure	1 atm

Two estimations were conducted using the model. As a first estimation, the heat transfer through the control volume boundaries was assumed to account only for the latent heat released from the steam condensation on the walls. The second estimation was performed accounting also for the natural convection heat transfer on the walls. It was verified that a significant amount of heat is released from the control volume by natural convection. The estimations based on the zero-dimensional model are summarized in Table 9:

**Table 9 : Summary of estimations by the zero-dimensional model**

<b>Estimation</b>	<b>Wall Boundary Condition</b>
E1	Steam condensation on the walls
E2	Steam condensation and natural convection on the walls

The following figures present the transients for condensed mass, temperature and pressure obtained by the simplified zero-dimension model:

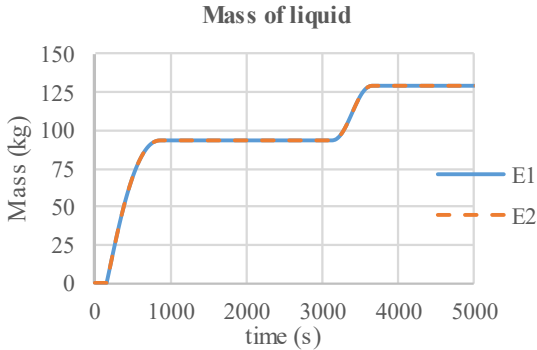


**Figure 9 – Mass of liquid transient obtained from the zero-dimensional model**

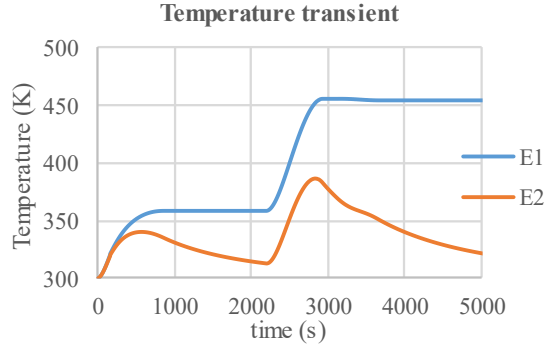


**Figure 10 – Temperature transient obtained from the zero-dimensional model**

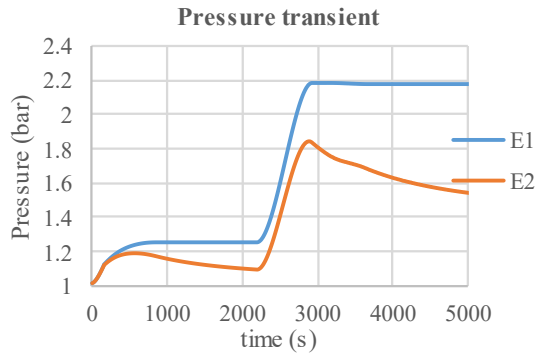


**Figure 11 – Pressure transient obtained from the zero-dimensional model**

It can be seen that there is no difference in the condensation of steam between the two simulations. This result could be anticipated, since the liquid mass in the control volume is assumed to depend on the saturation pressure of steam at the temperature of the wall, which is not affected by the differences of the two scenarios analyzed. In both simulations, the mass of steam that condenses is 129.2 kg, and the mass of saturated vapor that remains in the control volume is 24.5 kg.

### 4.3. CFD model

#### 4.3.1. Introduction

There are two main approaches to tackle the hydrogen distribution analysis in nuclear reactor containments. The most simplified one employs the use of lumped

parameter codes for the estimation of average thermodynamic properties at a few discrete locations during a transient accident. Due to its reduced computational cost, lumped parameter approach is suitable to be used for parametric analysis in which the influence of a parameter in the evolution of the accident is desired to be assessed. However, this is not the best approach to accurately predict hydrogen risk, since the coarse discretization cannot provide gases distribution inside the nodes [11]. Moreover, some aspects of the hydrogen transport phenomenon as buoyancy plumes and stratification must be accurately detailed using finer mesh grid and small time step to provide accuracy [8].

The second approach to model hydrogen transport is the use of CFD codes, which can provide more accurate estimations for the thermodynamic properties over all the containment geometry under a larger computational cost. There are CFD codes specifically designed to be applied for hydrogen study, as GASFLOW and CAST3M, which are fitted with built-in functions for recombiners modelling and steam condensation in the walls in the presence of non-condensable gases. Additionally, multi-purpose commercial CFD codes can also be used to model the hydrogen transport phenomena in nuclear containments, even though they would still require the implementation of suitable models for phenomena affecting hydrogen distribution.

The simulations performed throughout this thesis employ the commercial multi-purpose CFD code ANSYS Fluent, which should be complemented by the implementation of additional models. Boundary conditions as the mass and energy releases during the accident were extracted from references for the benchmark case analyzed, but they could also be generated using lumped parameter codes with reactor core simulating capabilities.

### 4.3.2. ANSYS Fluent capabilities and limitations

ANSYS Fluent is a commercial multi-purpose CFD code used for a large range of industrial applications. The code is applicable to modeling different flows and phenomena as single-phase flows, turbulent flows, multi-phase flows, and combustion. Moreover, Fluent allows the user to implement routines and coding macros in order to model phenomena that are not handled by the code by default.

Fluent solves numerically the conservation equations by resorting to the finite-volume approach in an either structured or unstructured mesh. The following equations represent the single-phase and multi-species conservations equations solved by the code [39]:

Mass conservation:

$$\frac{\partial \rho}{\partial t} + \nabla \cdot (\rho \vec{v}) = S_m \quad 51$$

Momentum conservation:

$$\frac{\partial}{\partial t}(\rho \vec{v}) + \nabla \cdot (\rho \vec{v} \vec{v}) = -\nabla p + \nabla \cdot (\bar{\tau}) + \rho \vec{g} + \vec{F} \quad 52$$

Energy conservation:

$$\frac{\partial}{\partial t}(\rho E) + \nabla \cdot (\vec{v}(\rho E + p)) = \nabla \cdot (k_{eff} \nabla T - \Sigma_j (h_j \vec{j}_j) + (\bar{\tau} \cdot \vec{v})) + S_h \quad 53$$

Species  $i$  conservation:

$$\frac{\partial}{\partial t}(\rho Y_i) + \nabla \cdot (\rho \vec{v} Y_i) = \nabla \cdot J_i + R_i + S_i \quad 54$$

Turbulent-kinetic energy conservation for standard k- $\epsilon$  turbulence model:

$$\frac{\partial}{\partial t}(\rho k) + \frac{\partial}{\partial x_i}(\rho k u_i) = \frac{\partial}{\partial x_j} \left[ \left( \mu + \frac{\mu_t}{\sigma_k} \right) \frac{\partial k}{\partial x_j} \right] + G_k + G_b - \rho \varepsilon - Y_M + S_k \quad 55$$

Turbulent dissipation rate conservation for standard k- $\varepsilon$  turbulence model:

$$\frac{\partial}{\partial t}(\rho \varepsilon) + \frac{\partial}{\partial x_i}(\rho \varepsilon u_i) = \frac{\partial}{\partial x_j} \left[ \left( \mu + \frac{\mu_t}{\sigma_\varepsilon} \right) \frac{\partial \varepsilon}{\partial x_j} \right] + C_{1\varepsilon} \frac{\varepsilon}{k} (G_k + C_{3\varepsilon} G_b) - C_{2\varepsilon} \rho \frac{\varepsilon^2}{k} + S_\varepsilon \quad 56$$

The analysis of a nuclear reactor accident requires the solution of the conservation equations for a two-phase model since a mixture of gaseous species (air, steam and hydrogen) and liquid water are present in the control volume. Thus, Equations 51, 52, and 53 are solved for each phase according to the Eulerian model, while the turbulent quantities in Equations 55 and 56 are shared for both phases. Equation 54 is solved for the species present in each phase, and the subscript index  $i$  represents the species. Equations 57, 58, and 59 replace the single-phase Equations 51, 52, and 53 for the Eulerian multi-phase model:

Mass conservation for phase  $q$ :

$$\frac{\partial}{\partial t}(\alpha_q \rho_q) + \nabla \cdot (\alpha_q \rho_q \vec{v}_q) = \sum_{p=1}^n (\dot{m}_{pq} - \dot{m}_{qp}) + \dot{S}_q \quad 57$$

Momentum conservation for phase  $q$ :

$$\begin{aligned} \frac{\partial}{\partial t}(\alpha_q \rho_q \vec{v}_q) + \nabla \cdot (\alpha_q \rho_q \vec{v}_q \vec{v}_q) = & -\alpha_q \nabla p + \nabla \bar{\tau}_q + \alpha_q \rho_q \vec{g} + \\ & \sum_{p=1}^n (\vec{R}_{pq} + \dot{m}_{pq} \vec{v}_{pq} - \dot{m}_{qp} \vec{v}_{qp}) + (\vec{F}_q + \vec{F}_{lift,q} + \vec{F}_{wl,q} + \vec{F}_{vm,q} + \vec{F}_{td,q}) \end{aligned} \quad 58$$

Energy conservation for phase  $q$ :

$$\begin{aligned} \frac{\partial}{\partial t} \left( \alpha_q \rho_q \left( e_q + \frac{\vec{v}_q^2}{2} \right) \right) + \nabla \cdot \left( \alpha_q \rho_q \vec{v}_q \left( h_q + \frac{\vec{v}_q^2}{2} \right) \right) = & \nabla \cdot (\alpha_q k_{eff,q} \nabla T_q - \sum_j h_{j,q} J_{j,q} + \\ & \tau_{eff,q} \cdot \vec{v}_q) + \sum_{p=1}^n (Q_{pq} + \dot{m}_{pq} h_{pq} - \dot{m}_{qp} h_{qp}) + p \frac{\partial \alpha_q}{\partial t} + S_q \end{aligned} \quad 59$$

Equations 57, 58, and 59 introduce the terms  $\dot{m}_{pq}$  and  $\dot{m}_{qp}$ . They stand for the phase change mass rate from phases  $p$  to  $q$ , and vice-versa. For the multi-phase transient analyzed, these terms represent the mass sinks and sources for liquid water and steam that reproduce condensation phenomenon. ANSYS Fluent is fitted with a condensation model to simulate bulk steam condensation, but there is no built-in function to model steam condensation in the presence of non-condensable gases, what will require the implementation of routines defined by the user to model this phenomenon.

Fluent uses the Lee Model [40] to simulate pure steam bulk condensation. This model can be summarized by rewriting Equation 57 by Equations 60 and 62. These equations represent the steam and liquid water mass conservation:

$$\frac{\partial}{\partial t}(\alpha_v \rho_v) + \nabla \cdot (\alpha_v \rho_v \rho \vec{v}_v) = \dot{m}_{lv} - \dot{m}_{vl} \quad 60$$

$$\frac{\partial}{\partial t}(\alpha_v \rho_v) + \nabla \cdot (\alpha_v \rho_v \rho \vec{v}_v) = \dot{m}_{lv} - \dot{m}_{vl} \quad 61$$

In the equations above, the terms  $\dot{m}_{lv}$  and  $\dot{m}_{vl}$  represent the evaporation and condensation mass rates, respectively. From Lee condensation model, these rates can be calculated by Equations 62 and 63, for a mixture only composed of steam and liquid..

$$\text{If } T_l > T_{sat}, \dot{m}_{lv} = K_e \alpha_l \rho_l \frac{T_l - T_{sat}}{T_{sat}} \quad 62$$

$$\text{If } T_v < T_{sat}, \dot{m}_{vl} = K_c \alpha_v \rho_v \frac{T_{sat} - T_v}{T_{sat}} \quad 63$$

When a fraction of liquid water in a cell receives heat from the adjacent cells or from the other species in the same cell and the final temperature of the liquid exceeds the saturation temperature of the water, the term  $\dot{m}_{lv}$  is included in Equations 60 and 62 to

represent phase change. This term corresponds to the evaporation mass rate and is proportional to the temperature difference  $T_l - T_{sat}$ , and also to the amount of liquid within the cell ( $\alpha_l \rho_l$ ). The process to represent condensation is analogous to the one described above for evaporation.

The model is based on mechanistic relaxation coefficients ( $K_e$  and  $K_c$ ), which have units of  $s^{-1}$ , and rule how fast the steam-liquid equilibrium is reached. The relaxation coefficients are related to rate at which a nonequilibrium mixture (such as the superheated steam released into the air mass inside the reactor containment) relaxes back to an equilibrium condition.

#### **4.3.3. Geometry modelling and Meshing**

For this analysis, the geometry of the marine reactor cabin presented by Zhao (2022) and Lyu (2020) will be used [13]. Limited information is found in the references about additional characteristics of the nuclear reactor and its containment. It is known that the cabin consists of a hexagonal compartment with 14 m of length, 10 m of width, and 8 m of height, and equipment main dimensions are also presented by these studies. However, equipment positioning in the cabin was extrapolated based on the figures provided.

Moreover, the distance between equipment and main dimensions of the pieces of equipment were adjusted in order to allow the utilization of uniform hexahedral meshes. Also, cylindrical shapes of equipment were modeled as hexahedrons with equal volume. This adjustment conserved the free volume of the cabin and the equipment volume.

The cabin is separated by a shielding structure, that divides the containment into two regions, the main cabin and auxiliary cabin. This structure was maintained during

geometry modelling, since it has influence on the hydrogen transport and accumulation in the containment. Figure 12 depicts the modelled geometry, and represents the main containment cabin in blue, separated from the auxiliary cabin, in green, by the shielding structure:

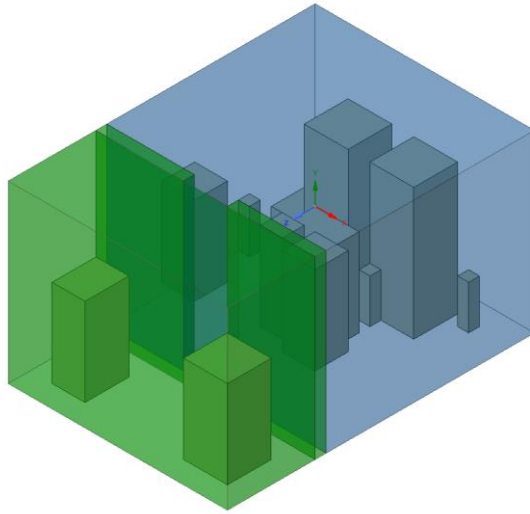


**Figure 12 – Modelled geometry**

Due to the adjustments in the containment and equipment geometry, optimized meshes were prepared using hexahedrons with 0.5, 0.25, and 0.125 m of length. Figure 13 presents the coarser mesh used for the simulations.

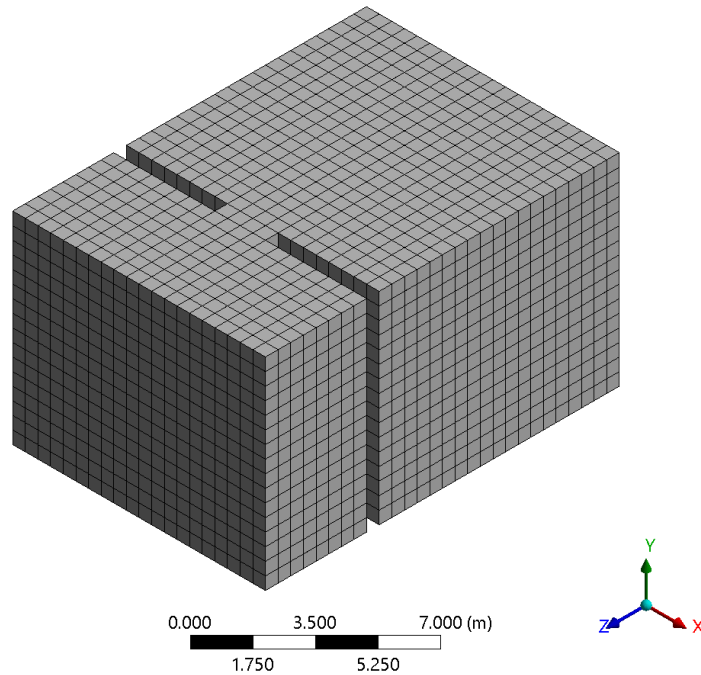


**Figure 13 – Base mesh (element size 0.5 m)**

Since the imposition of different boundary conditions is expected in different regions of the containment, the cells adjacent to the containment walls were separated from the interior of the containment geometry. This layer of cells is presented in Figure 14:

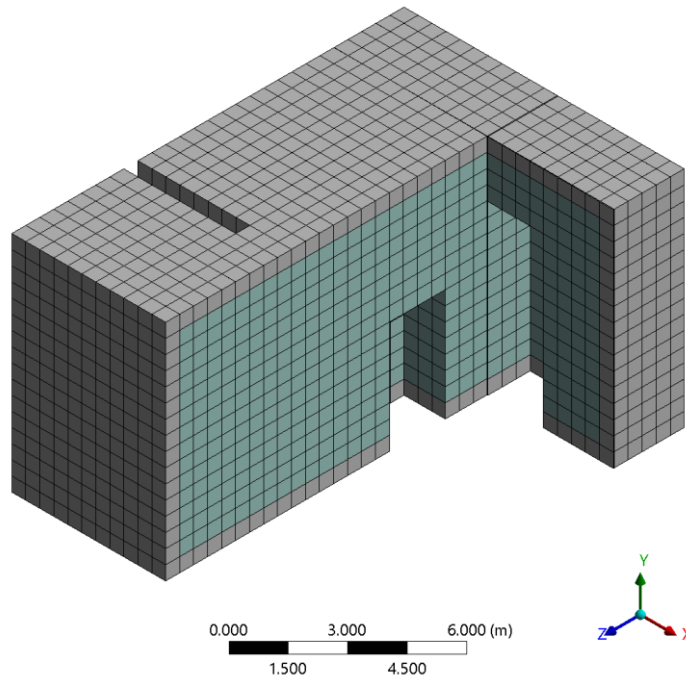


**Figure 14 – Wall layer mesh (gray)**

#### **4.3.4. Initial Conditions**

The containment initial conditions were initialized as obtained from the reference scenario adopted. The containment was assumed to be at 300K, 1 atm, and fully filled by air. These parameters represent the base scenario to be simulated. Additional simulations were performed to understand the specific parameters and models on the development of the accident.

#### **4.3.5. Boundary Conditions**

As an initial simplification for the simulation, the surfaces of equipment were modelled as adiabatic, while the containment walls were modelled to exchange heat with the adjacent compartments of the ship by natural convection. The natural convection heat transfer coefficients were imposed as boundary conditions to the vertical and horizontal

containment walls from Nusselt number empirical correlations for external free convection flows [15], as presented in Equations:

Vertical Surface:

$$\overline{Nu}_L = 0.68 + \frac{0.67Ra_L^{1/4}}{[1+(0.492/Pr)^{9/16}]^{4/9}} \quad (Ra_L < 10^9) \quad 64$$

Lower Surface of Cold Plate

$$\overline{Nu}_L = 0.54Ra_L^{1/4} \quad (10^4 < Ra_L < 10^7) \quad 65$$

$$\overline{Nu}_L = 0.15Ra_L^{1/3} \quad (10^7 < Ra_L < 10^{11}) \quad 66$$

Upper Surface of Cold Plate

$$\overline{Nu}_L = 0.27Ra_L^{1/4} \quad (10^5 < Ra_L < 10^{10}) \quad 67$$

Then, the natural convection heat transfer coefficient  $\bar{h}$  is obtained as:

$$\overline{Nu}_L = \frac{\bar{h}L}{k} \quad 68$$

Where  $L$  is the ratio between surface area and perimeter of the wall, and the Rayleigh number is calculated as:

$$Ra_L = \frac{g\beta(T_b - T_w)L^3}{\nu\alpha} \quad 69$$

Using the expressions above, the order of magnitude of the natural convection heat transfer coefficient can be estimated using the thermodynamic properties of the air, for a range of temperature differences, for the bottom, top and vertical walls of the containment. It can be anticipated that coefficients up to 10 W/m<sup>2</sup>K can be observed in the ceiling of the containment for extreme temperatures differences between the interior of the containment and the walls of 200°C.

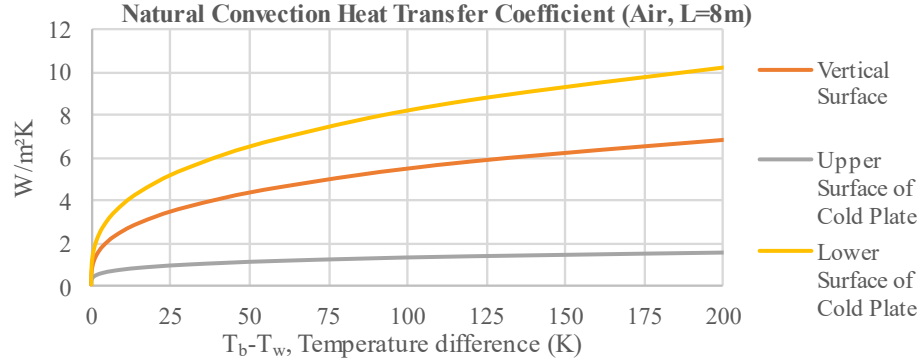


**Figure 15 – Natural convection heat transfer coefficients**

#### 4.3.6. Bulk Condensation Model

Due to the limitations of Fluent in-built condensation and evaporation model, presented in Section 4.3.2, the implementation of a model to account for the driver mechanism of steam partial pressure in the phase change was performed. This model follows the same strategy of introduction of mass source and sink terms in the phase conservation equations by the in-built model, but steam partial pressure is accounted for the condensation and evaporation conditions, and the steam weight fraction in the gas phase ( $W_{st,v}$ ) is introduced to calculate the steam sink ( $\dot{m}_{vl}$ ):

$$\text{If } T_l > T_{sat}(P_{st}), \dot{m}_{lv} = K_e \alpha_l \rho_l \frac{T_l - T_{sat}}{T_{sat}} \quad 70$$

$$\text{If } T_v < T_{sat}(P_{st}), \dot{m}_{vl} = K_c \alpha_v W_{st,v} \rho_v \frac{T_{sat} - T_v}{T_{sat}} \quad 71$$

This model assumes that in each cell, the species present (air, steam, and water) are mixed and the mixture will seek an equilibrium state with the different species at the same temperature. During a transient calculation, nonequilibrium conditions can occur because of changes in the system pressure, injection of steam, condensation of steam as a film on heat structures, and evaporation of liquid water from the film on heat structures.

The model predicts that the mixture of gases, steam, and water droplets will attempt to move back toward an equilibrium condition by either condensation of steam or evaporation of water. The rate at which the mixture approaches equilibrium is determined by water and steam concentrations in the cell, and the normalized temperature difference to the saturation point. The coefficients  $K_e$  and  $K_c$  represents the rate at which a nonequilibrium mixture returns to an equilibrium condition and were extracted from Lee Model [40].

#### 4.3.7. Wall Condensation Models

Due to the large volume of the geometry analyzed, the solution of the boundary layer adjacent to the walls for calculation of steam flux to the wall and heat transfer coefficients based on turbulent models would require a huge computational effort. To overcome this limitation, the modelling of condensation on the containment walls, accounting for the influence of the presence of non-condensable gases, can be performed by the addition of steam mass sinks and liquid water mass sources in the first layer of cells adjacent to the walls.

The modelling of these mass source and sink terms is based on the assumption that all the heat released from the condensation is released through the walls, and it is completely removed from the containment. The latent heat released from condensation can be expressed as a function of the condensation mass rate density ( $\dot{m}'''$ ):

$$q''' = h_{fg} \dot{m}''' \quad 72$$

Where  $h_{fg}$  is the latent heat of condensation, at the saturation temperature, and it has unit of J/kg. The condensation mass rate density is expressed in kg/(m<sup>3</sup>s), and the

released heat density ( $q'''$ ) in a wall-adjacent cell is expressed in W/m<sup>3</sup>. Although the heat released is a volumetric quantity, it is assumed to be totally rejected through the walls, since the wall condensation mechanism occurs in a surface interface. So, the heat released to the wall ( $q$ ) can be obtained by multiplying  $q'''$  by the volume of the cell ( $V_c$ ), and the heat flux by dividing the heat by the area that the cell shares with the wall ( $A_w$ ):

$$q'' = \frac{q}{A_w} = \frac{q'''V_c}{A_w} = q'''L \quad 73$$

Therefore, the equation above allows to express the condensation heat exchanged as a condensation heat transfer coefficient  $\bar{h}$ :

$$\bar{h} = \frac{q''}{T_b - T_w} \quad 74$$

Finally, the steam condensation mass volumetric rate ( $\dot{m}'''$ ) can be linked to the condensation heat transfer coefficient, by replacing Equations 73 and 74 in Equation 72:

$$\dot{m}''' = \frac{\bar{h} (T_b - T_w)}{h_{fg} L} \quad 75$$

For the implementation in the CFD simulation, a source condition is imputed in the wall adjacent layer zone of cells. The source term is introduced as calculated in Equation 75, in which the condensation heat transfer condition is obtained from the empirical correlations for wall condensation in the presence of non-condensable gases, described in Section 2.2.3.

It was verified that the introduction of the condensation mass source terms ( $\dot{m}'''$ ) in the cells adjacent to the walls made the solution diverge. To solve this inconvenience, Li (2013) used under-relaxation terms,  $\gamma$ , to make the solution stable [41]. This technique

modifies the source term,  $\dot{m}_n'''$ , by averaging the values obtained from Equation 75 for the current iteration with the source term from the previous iteration,  $\dot{m}_{n-1}'''$ , as presented by Equation 76:

$$\dot{m}_n''' = (1 - \gamma)\dot{m}_{n-1}''' + \gamma \left[ \frac{\bar{h} (T_b - T_w)}{h_{fg} L} \right] \quad 76$$

The under-relaxation factor ( $\gamma$ ) of 0.05 used by Li (2013) for modelling the condensation mass source term in vertical cylindrical condensers in the presence of non-condensable gases was adopted for this study.

#### 4.4. Definition of scenarios

The investigation of the hydrogen risk performed for this thesis was performed using different correlations for condensation on the walls. Experimental correlations based on Uchida's, Tagami's and Dehbi's experiments were used to model steam mass sinks and liquid water mass sources in the cells adjacent to the containment walls. During the literature review conducted, it was verified the conservatism of Tagami's correlation with regard to heat removal and overpressure limitation. However, the analysis was complemented by Dehbi's correlation which is suitable for condensation modelling since it accounts also for thermodynamic properties of the gaseous mixture and wall length, rather than only on the concentrations of non-condensable gases on the interface. Finally, due to its wide application in system level and hybrid codes, such as COMPACT, MAAP-DBA, and GOTHIC, Uchida's correlation was also selected to be applied.

Therefore, several simulations have been performed for the assessment of the influence of condensation correlation, time step, wall temperature, occurrence of liquid

reevaporating in the bulk of the containment, minimal residuals, maximum number of iterations, and relaxation factor for condensation mass source.

Table 10 summarizes the simulations performed through this thesis and their main boundary conditions. Results are presented in the next chapter.

**Table 10 : Summary of simulations performed by the CFD model**

Ref	Cell size (m)	Time step (s)	Wall BC	Wall condensation correlation	Bulk	Resid	T <sub>o</sub> (K)	T <sub>w</sub> (K)	K (s <sup>-1</sup> )	γ	Break
S1	0.500	0.100	Adiab.	Uchida	N	10 <sup>-5</sup> /10 <sup>-7</sup>	300	300	0.1	0.05	RPV
S2	0.500	0.100	NC	Uchida	N	10 <sup>-5</sup> /10 <sup>-7</sup>	300	300	0.1	0.05	RPV
S3	0.500	0.100	NC	Uchida	Y	10 <sup>-5</sup> /10 <sup>-7</sup>	300	300	0.1	0.05	RPV
S4	0.250	0.050	NC	Uchida	Y	10 <sup>-5</sup> /10 <sup>-7</sup>	300	300	0.1	0.05	RPV
S5	0.125	0.025	NC	Uchida	Y	10 <sup>-5</sup> /10 <sup>-7</sup>	300	300	0.1	0.05	RPV
S6	0.250	0.050	NC	Uchida	Y	10 <sup>-5</sup> /10 <sup>-7</sup>	300	300	0.1	0.05	RPV
S7	0.250	0.050	NC	Dehbi	Y	10 <sup>-5</sup> /10 <sup>-7</sup>	300	300	0.1	0.05	RPV
S8	0.250	0.050	NC	Tagami	Y	10 <sup>-5</sup> /10 <sup>-7</sup>	300	300	0.1	0.05	RPV
S9	0.250	0.050	NC	Uchida	N	10 <sup>-5</sup> /10 <sup>-7</sup>	300	300	0.1	0.05	RPV
S10	0.250	0.050	NC	Dehbi	N	10 <sup>-5</sup> /10 <sup>-7</sup>	300	300	0.1	0.05	RPV
S11	0.250	0.050	NC	Tagami	N	10 <sup>-5</sup> /10 <sup>-7</sup>	300	300	0.1	0.05	RPV
S12	0.250	0.050	NC	Dehbi	Y	10 <sup>-5</sup> /10 <sup>-7</sup>	288	288	0.1	0.05	RPV
S13	0.250	0.050	NC	Dehbi	Y	10 <sup>-5</sup> /10 <sup>-7</sup>	318	318	0.1	0.05	RPV
S14	0.500	0.100	NC	Dehbi	Y	10 <sup>-5</sup> /10 <sup>-7</sup>	300	288	0.1	0.05	RPV
S15	0.500	0.100	NC	Dehbi	Y	10 <sup>-5</sup> /10 <sup>-7</sup>	300	295	0.1	0.05	RPV
S16	0.500	0.100	NC	Dehbi	Y	10 <sup>-5</sup> /10 <sup>-7</sup>	300	300	0.1	0.05	RPV
S17	0.250	0.050	NC	Uchida	Y	10 <sup>-5</sup> /10 <sup>-7</sup>	300	300	0.1	0.05	PP
S18	0.500	0.100	NC	Uchida	Y	10 <sup>-5</sup> /10 <sup>-7</sup>	300	300	0.1	0.05	RPV
S19	0.500	0.100	NC	Uchida	Y	10 <sup>-5</sup> /10 <sup>-7</sup>	300	300	0.1	0.2	RPV
S20	0.500	0.100	NC	Uchida	Y	10 <sup>-5</sup> /10 <sup>-7</sup>	300	300	0.1	0.4	RPV
S21	0.500	0.100	NC	Uchida	Y	10 <sup>-4</sup> /10 <sup>-6</sup>	300	300	0.1	0.05	RPV
S22	0.500	0.100	NC	Uchida	Y	10 <sup>-5</sup> /10 <sup>-7</sup>	300	300	0.05	0.05	RPV
S23	0.500	0.100	NC	Uchida	Y	10 <sup>-5</sup> /10 <sup>-7</sup>	300	300	0.2	0.05	RPV

Bulk: Y (Bulk condensation evaporation model enabled)  
N (Bulk condensation evaporation model disabled)

T<sub>o</sub>: Initial containment temperature

T<sub>w</sub>: Containment wall temperature

K: Relaxation coefficients for condensation/evaporation

γ: Under-relaxation factor for wall condensation mass source

Break: RPV (longitudinal break at the Reactor Pressure Vessel)  
PP (longitudinal break towards the Primary Pump)

## 5. RESULTS

### 5.1. Comparison against zero-dimensional model

The first simulations performed using the methodology previously presented were compared against results obtained by the zero-dimensional model. It was anticipated that the transient behavior of the accident could not be accurately predicted, but for the long-term, the predictions of the zero-dimensional model should be trustful, so this first analysis aims to verify the CFD simulations capacity to minimally predict the final state of the accident.

Since the zero-dimensional model relies on mass and energy conservation equations, after a sufficiently long amount of time since the last release of steam and hydrogen occurs, it is expected that the accident would reach a steady state. For this analysis, two scenarios were simulated. S1 was performed using the same boundary conditions defined for E1 from the zero-dimension model. For this comparison, the heat removal through containment walls can occur only by the heat released from steam condensation. Although this boundary condition is unrealistic, it would still allow the verification about the simulation capabilities without introducing uncertainties about the natural convection modelling on the walls.

A second comparison was conducted by allowing also heat transfer on the walls by natural convection, as described in Section 4.3.5. The natural convection average heat transfer coefficients are calculated from the same correlations, though for the CFD

simulation they are assessed at each cell on the wall and for the zero-dimension model, a single coefficient is used for all the control volume external surface.

The following plots present the comparison between the CFD simulations against the zero-dimensional models. It could be verified as anticipated, that the agreement between both models should be higher when the accident reached the steady-state.

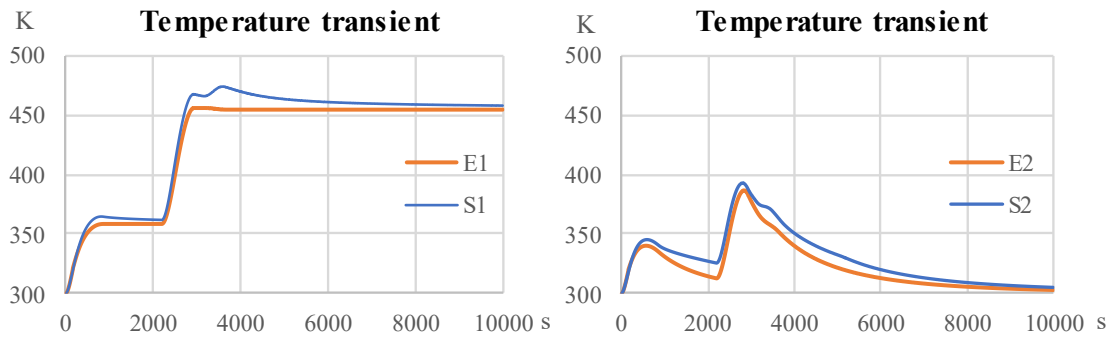


**Figure 16 – Temperature transient from E1, S1, E2, and S2**

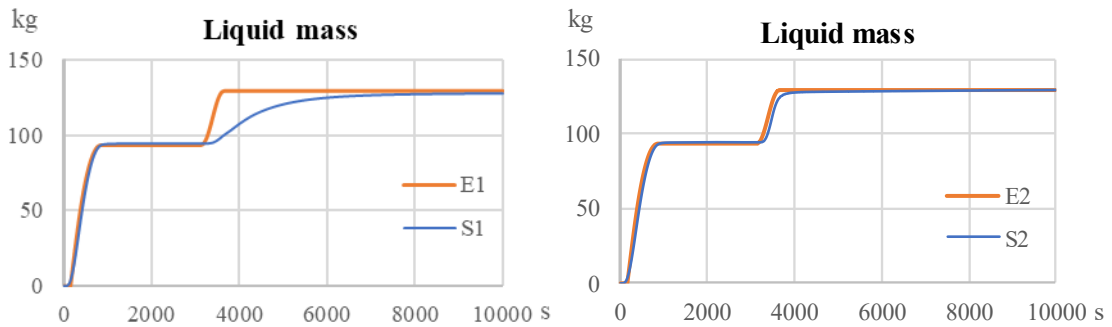


**Figure 17 – Liquid mass transient from E1, S1, E2, and S2**

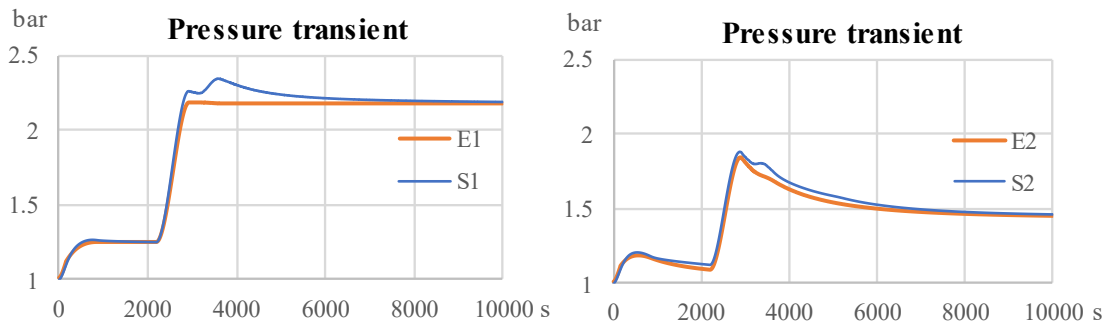


**Figure 18 – Pressure transient from E1, S1, E2, and S2**

Table 11 summarizes the results obtained by S1 and E1. It was verified a reasonable agreement between the zero-dimension model and the CFD simulations. The zero-dimensional model and the simulation presented deviations mostly during the transient, rather than the end of the accident. An average deviation of 2.0% was verified for S1 temperatures, while -2.7% was obtained for liquid masses and 3.1% for pressures, with regard to the values provided by E1.

**Table 11 : Comparison between zero-dimensional and CFD models (E1 and S1)**

	<b>Max Temperature</b>	<b>Final Temperature</b>	<b>Final mass of liquid water</b>	<b>Max Pressure</b>	<b>Final Pressure</b>
E1	456 K	454 K	129.1 kg	2.18 bar	2.18 bar
S1	474 K	460 K	127.6 kg	2.37 bar	2.22 bar
Deviation	4.0%	1.3%	-1.2%	8.7%	1.8%

Table 12 summarizes the results obtained by S2 and E2. An average deviation of 2.4% was verified for S1 temperatures, while 0.1% was obtained for liquid masses and 1.8% for pressures, with regard to the values provided by E1.

**Table 12 : Comparison between zero-dimensional and CFD models (E2 and S2)**

	<b>Max Temperature</b>	<b>Final Temperature</b>	<b>Final mass of liquid water</b>	<b>Max Pressure</b>	<b>Final Pressure</b>
E2	386 K	303 K	129.2 kg	1.84 bar	1.45 bar
S2	400 K	305 K	129.2 kg	1.88 bar	1.46 bar
Deviation	3.5%	0.7%	0.004%	2.0%	0.7%

These differences in the transient behavior can be explained from the fact that the condensation hypothesis in the simplified model cannot model accurately the transient condensation in the control volume, what led to lower average temperatures when steam was assumed to promptly condenses on the walls, removing heat from the control volume. This conclusion can be verified from the two pairs of scenarios compared, but it is the main reason from the differences seen in the transients of E1 and S1.

The differences verified in the temperature transients of E2 and S2 are also a result of the modelling of heat removal by natural convection on the walls. Three different empirical correlations were used to average an overall heat transfer coefficient on the walls, as presented in Section 4.3.5. Nevertheless, the treatment used to represent the temperature of the control volume by a single value of temperature is not realistic, since in a real containment during a transient release of steam and hydrogen, different flow temperatures can be expected over the different walls, even though natural convection shall dominate the flow pattern.

Finally, differences in the temperature transients between the zero-dimension model and CFD simulations can also come from the fact that the average temperatures obtained from CFD are calculated by averaging the values from all the cells in the grid. On the other hand, the single temperature value from the zero-dimension model, obtained theoretically, is rather a weighted-average value with regard to the thermal capacity of the species it contains.

The zero-dimensional model proposed does not ambition to estimate accurately the whole progression of the transient, since it relies on prompt condensation of the amount

of steam that overcomes the saturation pressure, and that heat is efficiently exchanged among the species of the control volume. Nevertheless, since it is based on energy and mass conservation equations, it is expected to provide more accurate results as the control volumes approached a steady state. Therefore, the final estimations obtained for the transient temperature and pressures are assumed to be realistic, and the results obtained by CFD simulations for the end of the transient should approach this estimation.

## **5.2. Grid convergence analysis**

The effect of the refinement of mesh used on the solution obtained was verified by a grid sensitivity analysis performed according to the ASME V&V 20 [42]. The convergence assessment of the solution was verified for three different mesh refinements of 0.5, 0.25 and 0.125 m.

It must be highlighted that the size of the cells is not the only difference among the meshes analyzed. The condensation phenomenon on the walls is modelled by the addition of liquid mass sources and steam mass sinks in the wall adjacent layer of cells. If the size of the wall layer of the mesh was preserved for the most refined meshes, more than one layer of cells should be defined with the condensation condition, what would trigger condensation before the steam reaches the cold surfaces of the walls. Therefore, the grid sensitivity analysis accounts not only for different cell sizes, but also different wall layers for the imposition of the condensation mechanism on the walls. The different meshes used for the grid convergence analysis are presented in Figures 19 and 20.

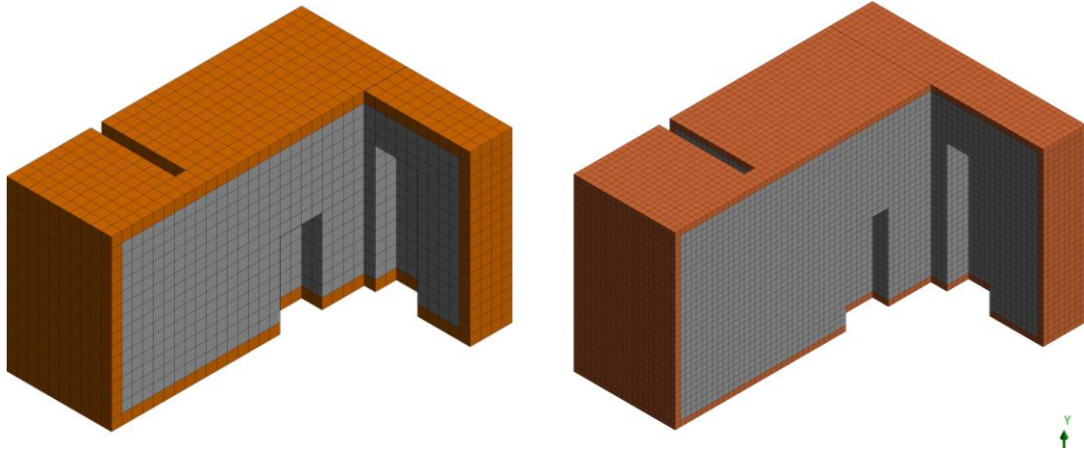


Figure 19 – Meshes M3 (0.5 m) and M2 (0.25 m)

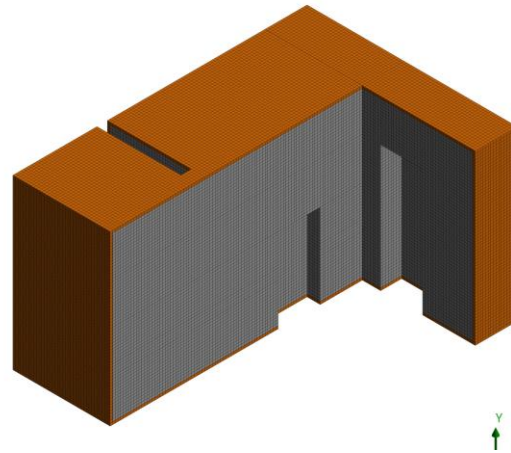


Figure 20 – Mesh M1 (0.125 m)

Table 13 presents the characteristics of the meshes employed for the grid sensitivity analysis:

**Table 13 : Characteristics of meshes employed**

Mesh	Topology	Cell Size (m)	Number of cells
M1	Hexahedral	0.125	495,872
M2	Hexahedral	0.250	61,984
M3	Hexahedral	0.500	7,748

Due to the huge computational effort required for the simulations of the most refined mesh, the grid sensitivity analysis was performed up to 300 s of transient. At this time, the convergence of important parameters for the development of the transient should be verified. It was selected for this analysis the average temperature, condensed mass and average total pressure, since even for this reduced transient, these parameters are directly affected by the condensation mechanism, which it is desired to assess if the utilization of different grids and wall layers could affect the solution.

According to ASME V&V 20 [42], the observed power order of convergence can be calculated based on the variations between the observed quantity  $\phi$  assessed at different grids, and can be calculated by Equations 77 and 78:

$$p = \frac{1}{\ln(r_{21})} \left[ \ln \left| \frac{\phi_3 - \phi_2}{\phi_2 - \phi_1} \right| + q(p) \right] \quad 77$$

$$q(p) = \ln \left( \frac{r_{21}^p - s}{r_{32}^p - s} \right) \quad 78$$

Where  $r_{21}$  is the ratio between the size of cells of grids 2 and 1,  $r_{32}$  is the ratio between the size of cells of grids 3 and 2, and  $s$  is calculated as:

$$s = \text{sign} \left( \frac{\phi_3 - \phi_2}{\phi_2 - \phi_1} \right) \quad 79$$

For the above definitions, the grid 1 is assumed to be the finer, and the grid 3 is assumed to be the coarser. Thus,  $\phi_3$  represents the value of the observed quantity obtained by the simulation using the grid 3.

Finally, the convergence can be assessed by evaluation of the ratio between the increment of the observed quantities after the simulation using three different grids. If

convergence is verified, then the difference between the observed quantity for the finer and intermediate mesh must be lower than the difference observed by the difference between the intermediate and coarser mesh. This ratio is called discriminating ratio ( $R$ ) and can be calculated as:

$$R = \frac{\phi_2 - \phi_1}{\phi_3 - \phi_2} \quad 80$$

The convergence assessment can be verified using the discriminating ratio [43]:

If  $0 < R < 1$ , monotonic convergence.

If  $R > 1$ , monotonic divergence.

If  $R < 0$  and  $|R| < 1$ , oscillatory convergence.

If  $R < 0$  and  $|R| > 1$ , oscillatory divergence.

The following figures represent the transient for the observed quantities (pressure, temperature and mass of liquid) for the three different meshes.

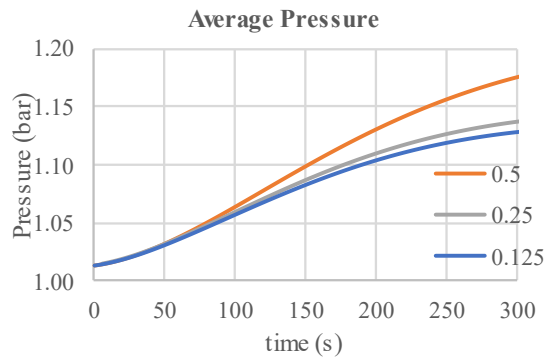


**Figure 21 – Pressure transient from S3, S4, and S5**

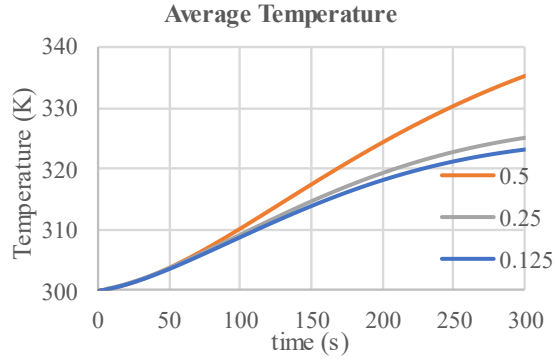


**Figure 22 – Temperature transient from S3, S4, and S5**

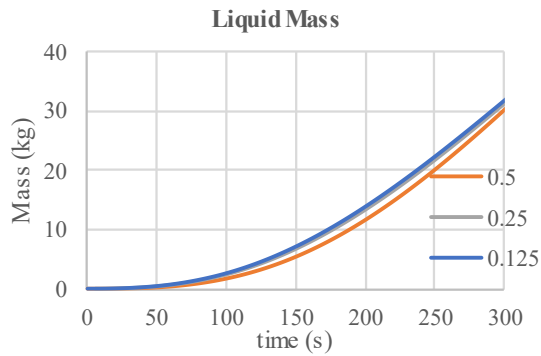


**Figure 23 – Water liquid mass transient in the containment from S3, S4, and S5**

It can be seen that the first refinement conducted, by moving to the mesh M2, produced significantly lower temperatures and pressures. However, an additional refinement to the mesh M3, led to marginal accuracy increase. The observed quantities simulated at 300 seconds and the parameters obtained by the grid convergence analysis are summarized in Table 14:

**Table 14 : Summary of simulations for grid convergence analysis**

	<b>Temperature (at 300s)</b>	<b>Pressure (at 300s)</b>	<b>Mass of liquid (at 300s)</b>
S3 (M3 0.500 m)	335.2 K	1.175 bar	30.2 kg
S4 (M2 0.250 m)	325.0 K	1.137 bar	31.1 kg
S5 (M1 0.125 m)	323.2 K	1.129 bar	32.0 kg
Power order of convergence, p	2.45	2.23	0.13
Discriminating ratio, R	0.18	0.21	0.91
Convergence assessment	Monotonic convergence	Monotonic convergence	Monotonic convergence
Approximate relative error (M2)	3.1 %	3.3 %	3.0 %
Grid convergence index (M2)	3.9 %	4.2 %	3.7 %

The simulation of the transient of 300 s using M3 required 11.7 hours to be performed using 16 cores, while using M2 and M1 required 22.5 and 153.8 hours to be performed using 32 cores (Intel Xeon 6248R 3.0 GHz).

### **5.3. Comparison of condensation correlations**

Simulations S6, S7 and S8 were performed to verify the influence of the empirical condensation correlations on the hydrogen combustion regimes. Three empirical correlations were selected to be employed in this analysis: Uchida, Dehbi and Tagami's correlations. It could be anticipated that Tagami's correlation should be the most conservative with regard to heat removal, since it provides the lowest heat transfer coefficients for the range of non-condensable mass fractions analyzed. The utilization of Dehbi's correlation was justified by the large range of parameters it was proposed for, and Uchida's by its utilization in many reactor safety codes. The figures below present a comparison of average temperature and liquid water mass evolution in the containment during the transient analyzed:

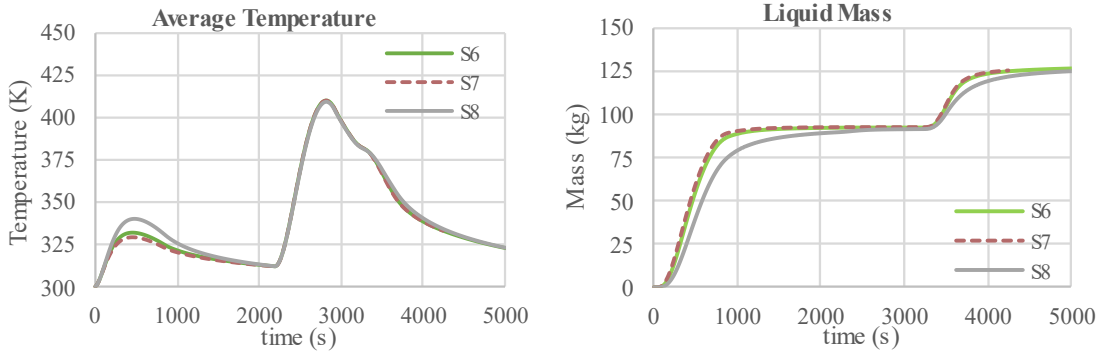


**Figure 24 – Temperature and liquid mass transient from S6, S7, S8**

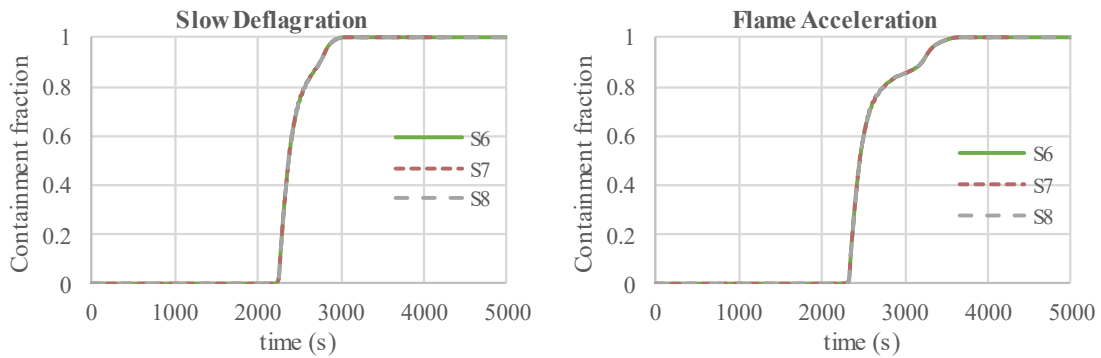


**Figure 25 – Fraction of the containment under SD and FA risk from S6, S7, S8**

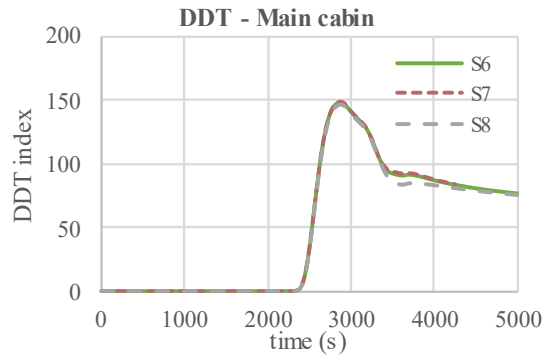


**Figure 26 – Average DDT index in the main cabin from S6, S7, S8**

Table 15 summarizes the instants when the whole containment reached the possibility of undergoing slow deflagration, flame acceleration and the maximum DDT index verified for the main cabin:

**Table 15 : Summary of simulations for comparison of condensation correlations**

Sim.	Instant when the whole containment is under SD risk	Instant when the whole containment is under FA risk	Max. DDT index in back cabin	Max. DDT index in main cabin
S6	3059 s	3660 s	116.1 at 2851 s	148.2 at 2872 s
S7	3060 s	3657 s	116.3 at 2850 s	148.5 at 2872 s
S8	3055 s	3661 s	114.6 at 2853 s	146.3 at 2874 s

It can be observed that the utilization of different empirical correlations to model the condensation on the walls led to different average temperatures in the containment, as a result of different condensation rates on the walls. As it could be anticipated, Tagami's correlation provided the lowest condensation rates, what was responsible by the lower heat removal and the larger average temperatures verified. With regard to the combustion regimes, no significant difference was verified by the utilization of different correlations. All the simulations showed that the containment has met the criteria for occurrence of SD, FA and DDT during the progression of the accident.

These simulations predicted that about 3060 s, the whole containment would be under the risk of SD, and about 3660 s, under the risk of FA, as shown in Table 15.

#### **5.4. Effect of bulk condensation and evaporation**

Simulations S9, S10 and S11 were performed to verify the influence of bulk condensation and evaporation in the interior of the on the hydrogen combustion regimes. These simulations were based on the ones described in Section 5.3, but they differ from them by not allowing phase change from bulk condensation or evaporation in the interior of the containment. Therefore, the implemented mechanism described in Section 4.3.6 was not defined for this set of simulations, only the wall condensation mechanism presented in Section 4.3.7.

The same conclusions obtained for the comparison of condensation correlations can be verified when condensation and evaporation are not allowed in the interior of the containment, as it can be seen in Figure 27. When steam and water phase change is neglected in the interior of the containment, Tagami's correlation also provided slower condensation rate and heat transfer on the walls, and slightly higher average temperatures, since the slower condensation also removes heat more slowly through the containment walls.

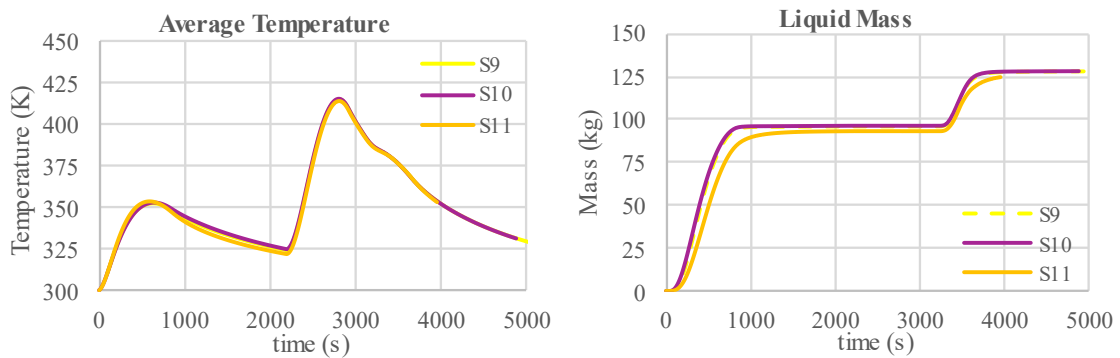


**Figure 27 – Temperature and liquid mass transient from S9, S10, S11**

Some interesting conclusions can be obtained by the comparison of the results for the same condensation correlation for the two different scenarios of phase change in the interior of the containment. Figures 28, 29, 30 and 31 present a comparison of the evolution of average temperature, mass of liquid, average steam mole fraction and combustion regimes in the containment for simulations in which phase change in the interior of the containment was neglected and accounted for. For this comparison, the same empirical correlation for condensation was imposed on the walls. The results presented by the following figures were obtained using Uchida's empirical correlation, but their behavior and trends were also verified for Tagami's and Dehbi's correlations:

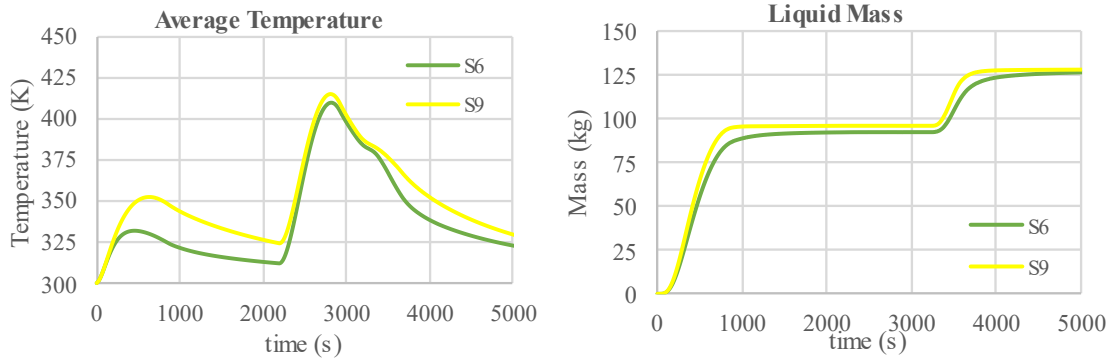


**Figure 28 – Temperature and liquid mass transient from S6 and S9**

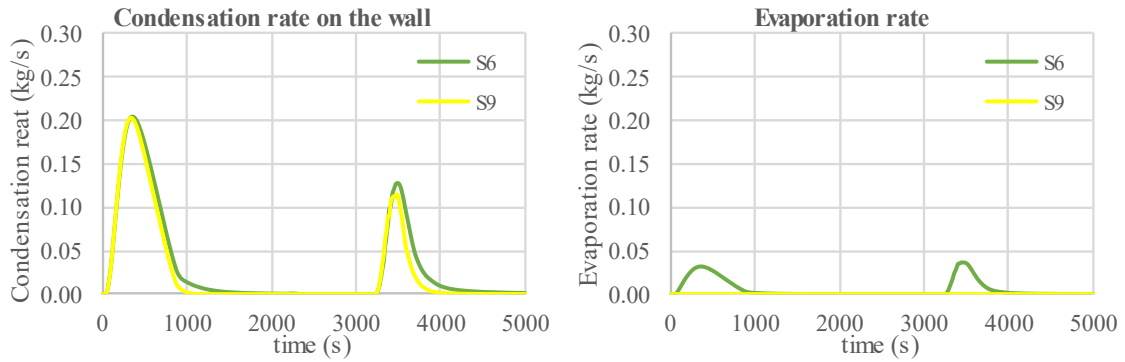


**Figure 29 – Condensation rate and Average steam mole fraction from S6 and S9**

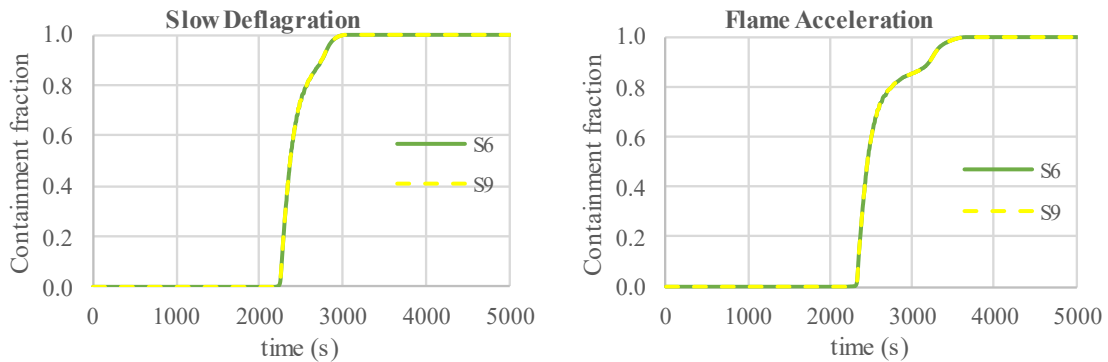


**Figure 30 – Fraction of the containment under SD and FA risk from S6 and S9**

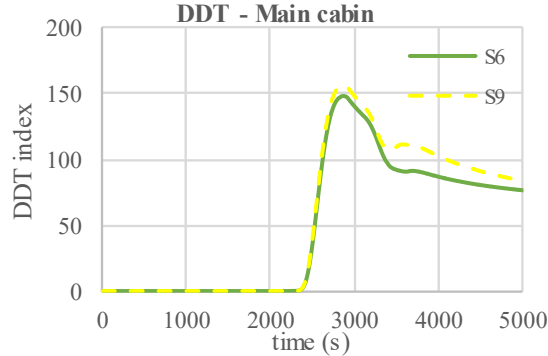


**Figure 31 – Average DDT index in the main cabin from S6 and S9**

It was verified that the phase change in the interior of the containment was able to reduce the average temperature in the containment. The observed average temperature reductions were up to 20.5 K and 13.6 K, in the first 2000 s of accident, when Uchida’s (S6 and S9) and Tagami’s (S8 and S11) correlation were employed, respectively. Little influence of the bulk condensation and evaporation was noticed on the SD and FA combustion regimes. It was observed that when bulk condensation and evaporation are accounted for, the instant in which the whole containment can undergo SD and FA is not significantly affected. With regard to DDT, the influence of bulk phase change did not affect the likelihood of detonation, but the increase in the temperatures observed when bulk phase change was neglected, made the DDT index higher.

Table 16 summarizes the results obtained from this comparison:

**Table 16 : Summary of simulations for comparison of influence of bulk phase change**

Sim.	Instant when the whole containment is under SD risk	Instant when the whole containment is under FA risk	Max. DDT index in back cabin	Max. DDT index in main cabin	Max. Containment Temperature
S6	3059 s	3660 s	116.1 at 2851 s	148.2 at 2872 s	409.8 K at 2820 s
S9	3058 s	3676 s	122.5 at 2847 s	156.4 at 2870 s	415.0 K at 2812 s

## 5.5. Effect of wall and initial temperatures

Simulations S7, S12, S13, S14, and S15 were performed to verify the influence of wall temperatures and containment initial temperatures on the hydrogen combustion regimes. These simulations were performed using Dehbi's empirical correlation for wall condensation, since it accounts for different condensation heat transfer coefficients for different wall temperatures. Figures 32, 33, 34, and 35 present the evolution of average temperature, liquid mass, condensation rate on the walls, and the risk of each combustion regime for each wall and initial temperatures simulated.

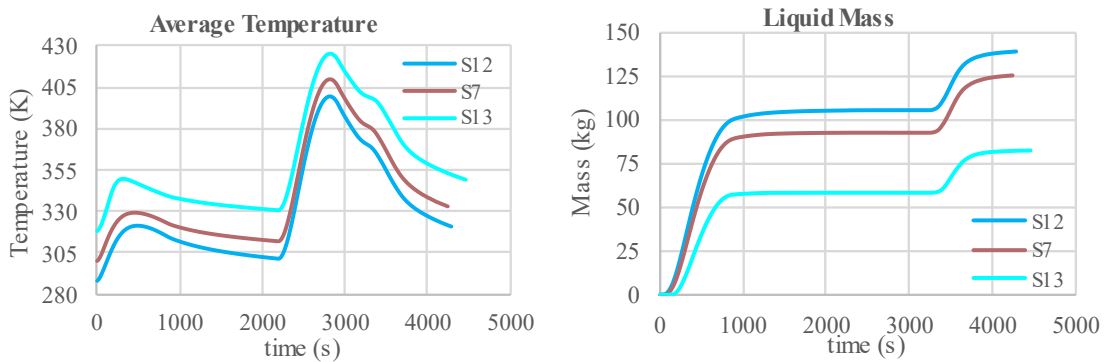


Figure 32 – Temperature and liquid mass transient from S7, S12, and S13

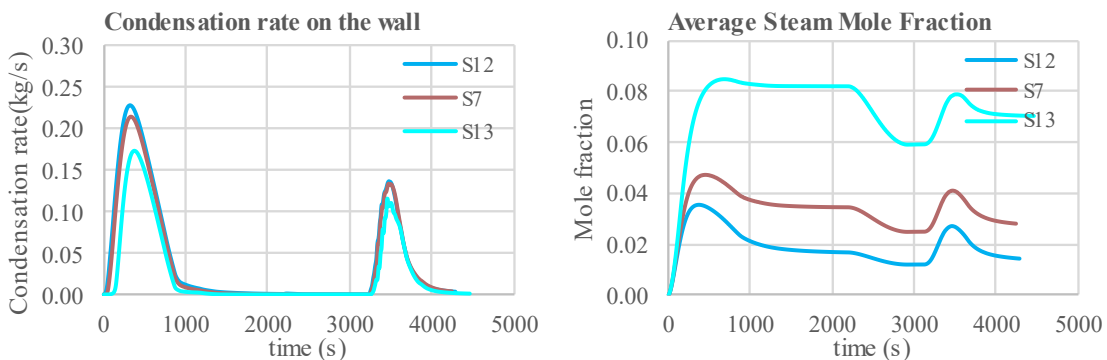
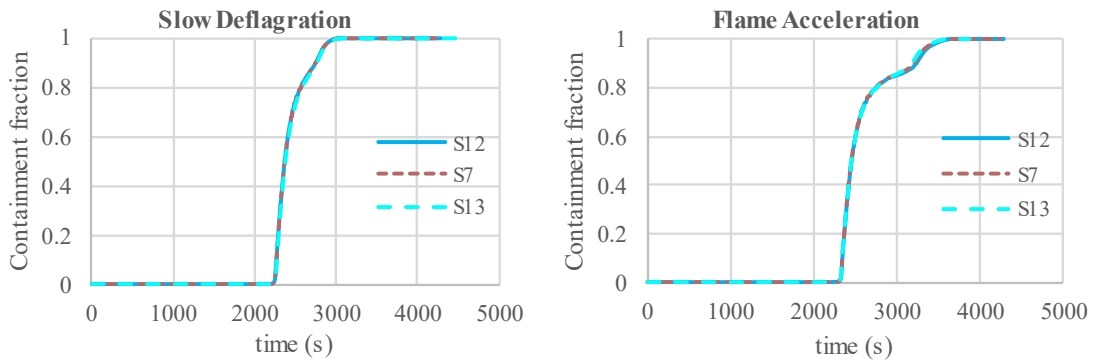
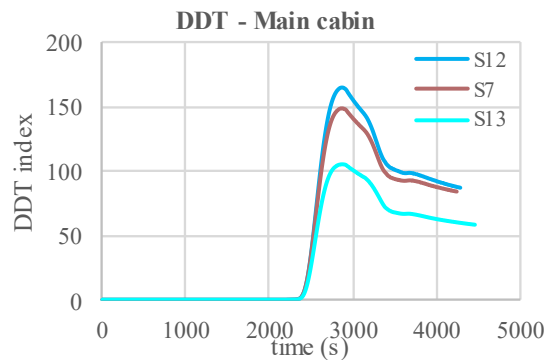


Figure 33 – Condensation rate and average steam fraction from S7, S12, and S13



**Figure 34 – Fraction of the containment under SD and FA risk from S7, S12, and S13**



**Figure 35 – Average DDT index in the main cabin from S7, S12, and S13**

Table 17 summarizes the results obtained by the simulations of different containment wall and initial temperatures:

**Table 17 : Summary of simulations for assessment of the effect of wall temperature**

Sim.	Instant when the whole containment is under SD risk	Instant when the whole containment is under FA risk	Max. DDT index in back cabin	Max. DDT index in main cabin	Max. Containment Temperature
S7	3060 s	3657 s	116.3 at 2850 s	148.5 at 2872s	409.7 K at 2819 s
S12	3058 s	3672 s	128.9 at 2859 s	164.7 at 2873 s	399.4 K at 2818 s
S13	3074 s	3654 s	82.55 at 2836 s	105.1 at 2874 s	425.2 K at 2823 s

It can be verified that different initial and wall temperatures did not affect the achievement of combustion regimes, nor were able to significantly postpone the instant when the whole containment would be under SD and FA risk.

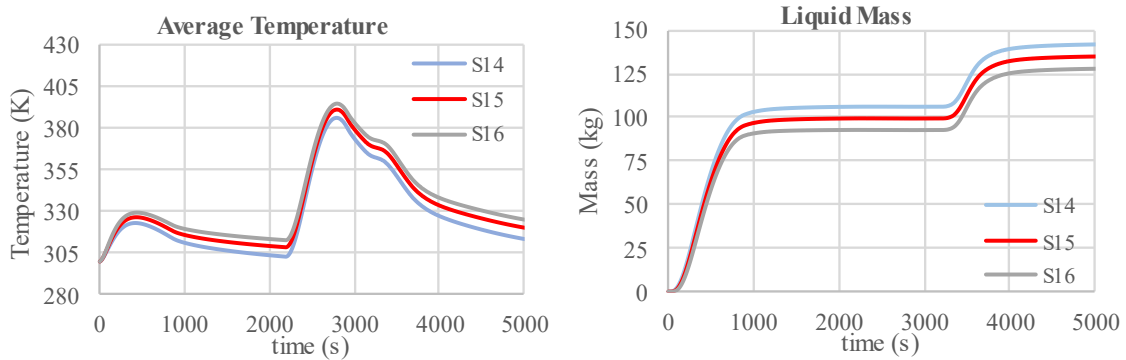


Figure 36 – Temperature and liquid mass transient from S7, S14, and S15

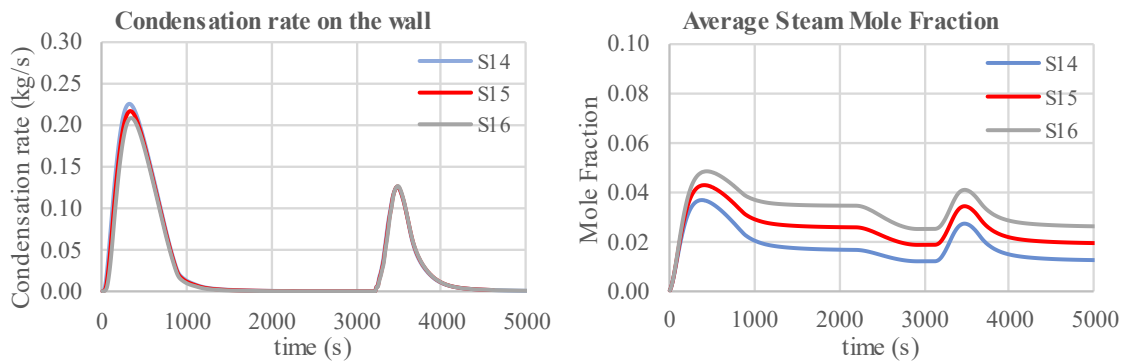


Figure 37 – Condensation rate and average steam fraction from S7, S14, and S15

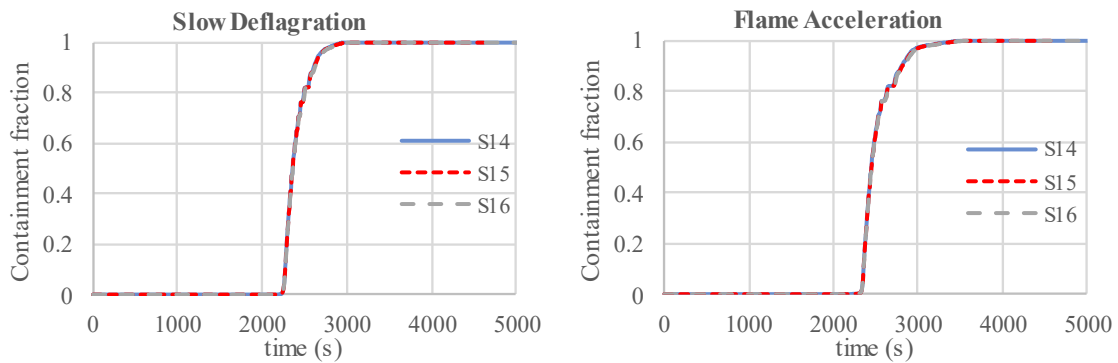
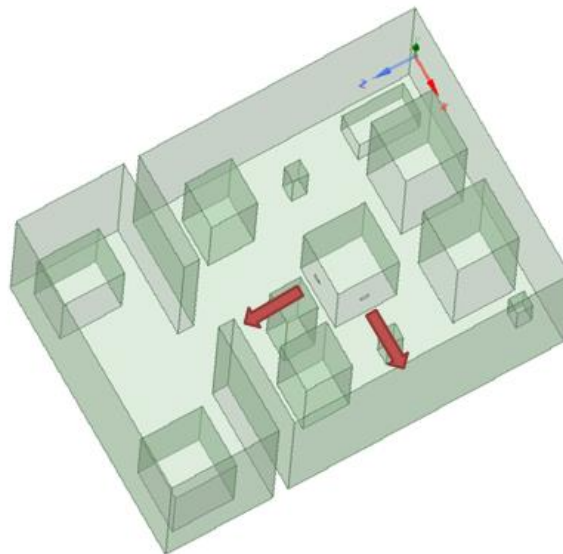


Figure 38 – Fraction of the containment under SD and FA risk from S7, S14, and S15

A similar analysis was performed to account for different wall temperatures, in order to remove the influence of the initial temperature of the interior of the containment, S14 and S15 were initialized at the same temperature of 300K, but the boundaries of the domain were maintained at different wall temperatures (288K and 295K).

### **5.6. Effect of the position of the leak**

Simulations S6 and S17 were performed to verify the influence of the positioning of the break in the primary system on the hydrogen distribution and combustion regimes. S15 simulated the steam and hydrogen release in the longitudinal direction of the cabin, while S16 the release was made towards the side walls. Figure 39 indicates the positioning of the steam and hydrogen releases for S15 and S16, and Figures 40, 41, and 42 depict the transient evolutions of average temperatures, mass of condensed water, and the possibilities of each combustion regimes.



**Figure 39 – Positioning of the breaks in the primary circuit for S6 and S17**

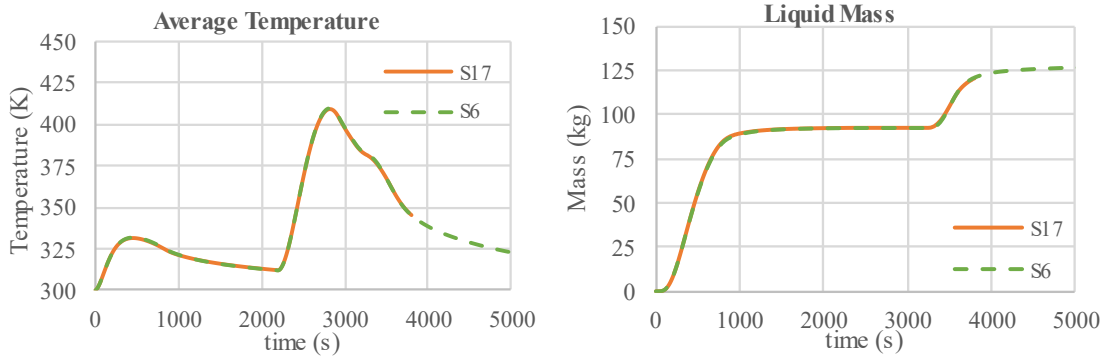


**Figure 40 – Temperature and liquid mass transient from S6 and S17**

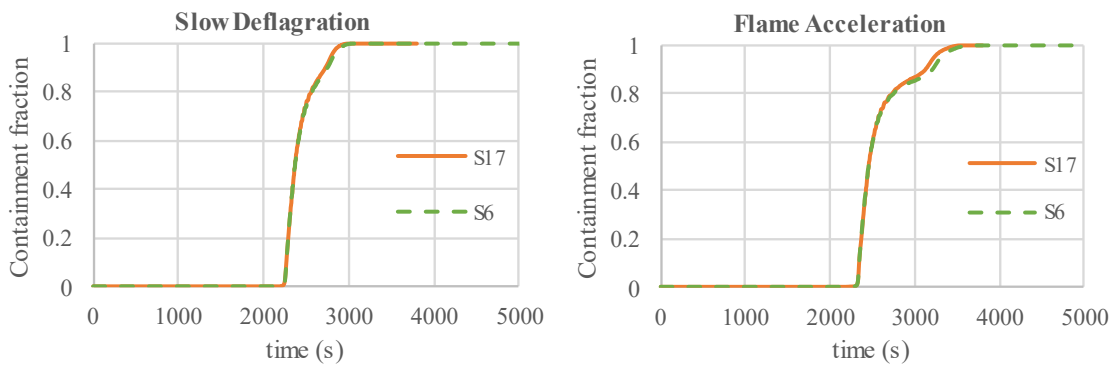


**Figure 41 – Fraction of the containment under SD and FA risk from S6 and S17**

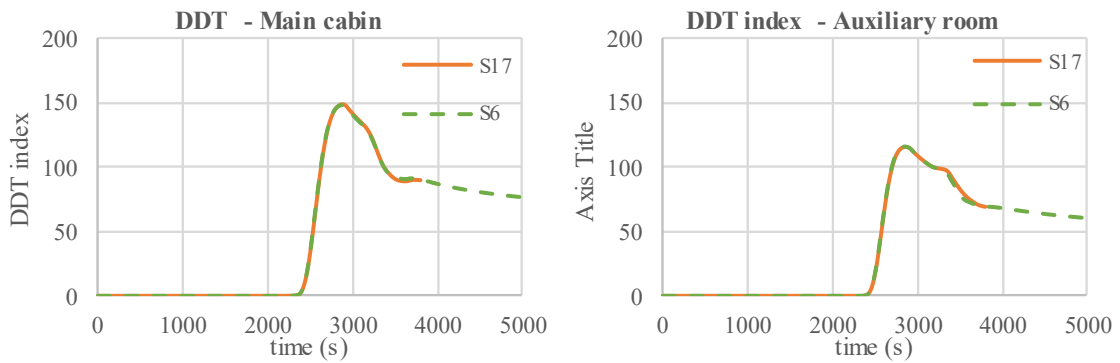


**Figure 42 – Average DDT index in the main and auxiliary cabin from S6 and S17**

## 5.7. Numerical Analysis

### 5.7.1. Under-relaxation factors for condensation mass sources

Simulations S18, S19 and S20 were performed to verify the influence of the under-relaxation factors ( $\gamma$ ) for the condensation mass source implemented on the walls. The under-relaxation factors analyzed were 0.05, 0.2, and 0.4. It was verified that the choice of this parameter did not affect the results, as seen in Figures 43 and 44, but they were necessary in order to obtain a stable solution. It was also verified that the choice of lower factors required a higher number of iterations per time step in order to achieve the residuals convergence criteria, as presented in Figure 45.

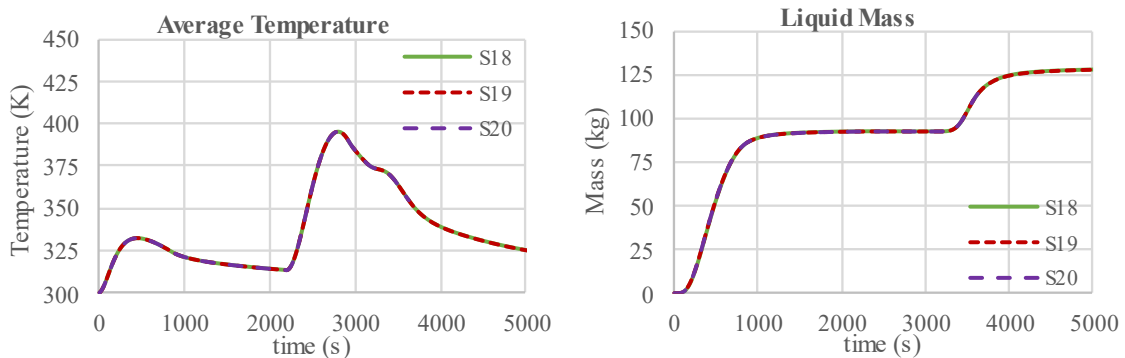


Figure 43 – Temperature and liquid mass transient from S18, S19, and S20

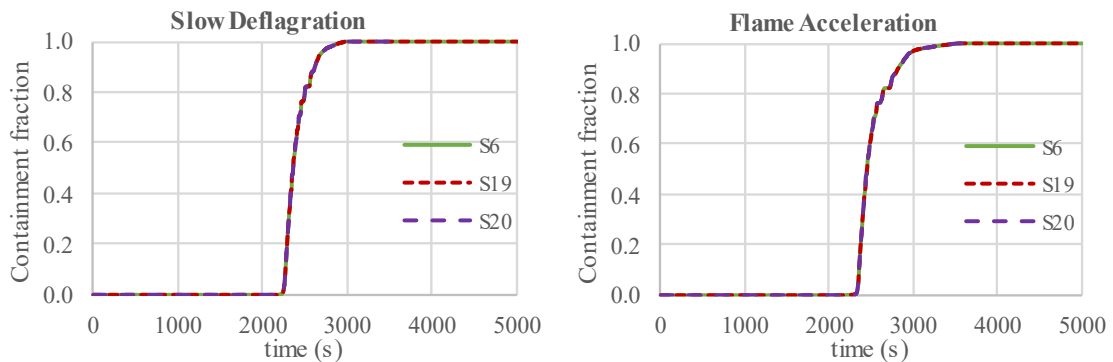
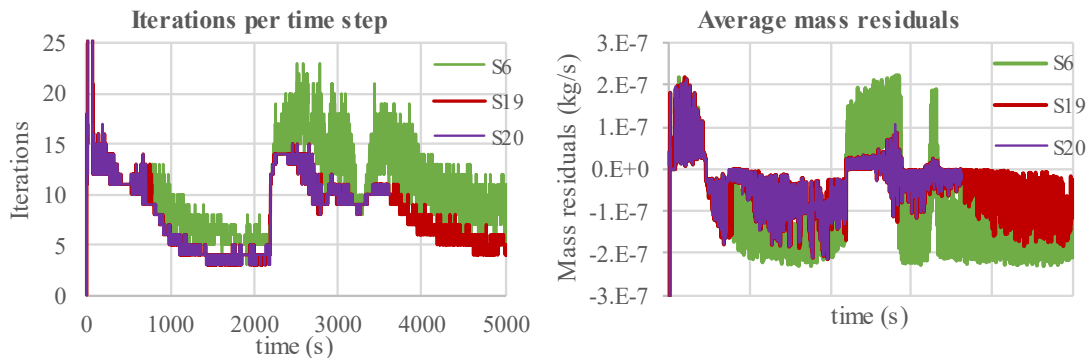


Figure 44 – Fraction of the containment under SD and FA risk from S18, S19, S20



**Figure 45 – Iterations required per time step and residuals for S18, S19, and S20**

### 5.7.2. Residuals

Simulations S18 and S21 were performed to verify the influence of the maximum residuals defined for convergence of the solution for each time step. For Simulation S18, each time step was assumed to converge when the quantities residuals reached values below  $10^{-5}$  for mass, momentum, phase volume fraction, species mass fraction, and turbulent quantities, and  $10^{-7}$  for energy, while for S21, the maximum residuals for convergence were  $10^{-6}$  for energy, and  $10^{-4}$  for the other quantities. Figure 46 presents the average temperature of the containment and condensation rate on the walls during the transient, and Figure 47 presents the number of iterations per time step required for convergence and average mass residuals:

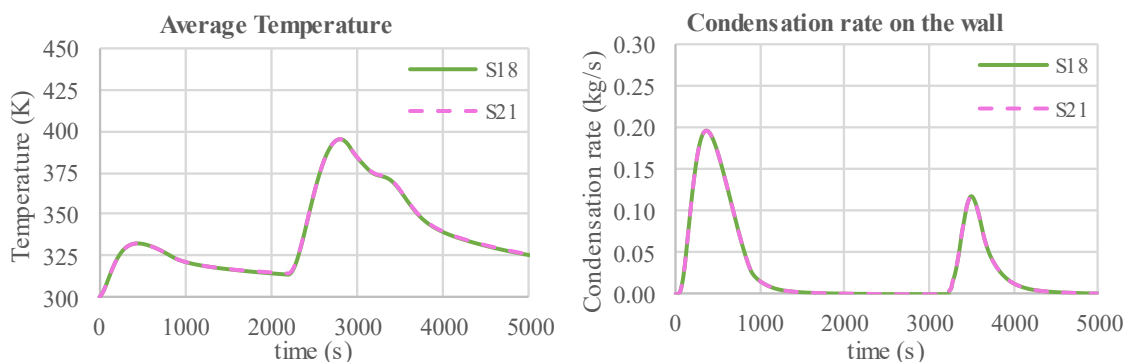


**Figure 46 – Temperature and condensation rate transient from S18 and S21**

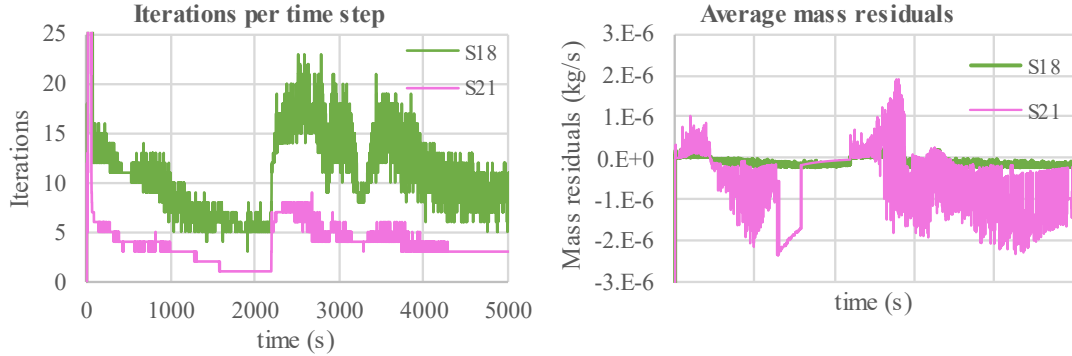


**Figure 47 – Iterations required per time step and residuals from S18 and S21**

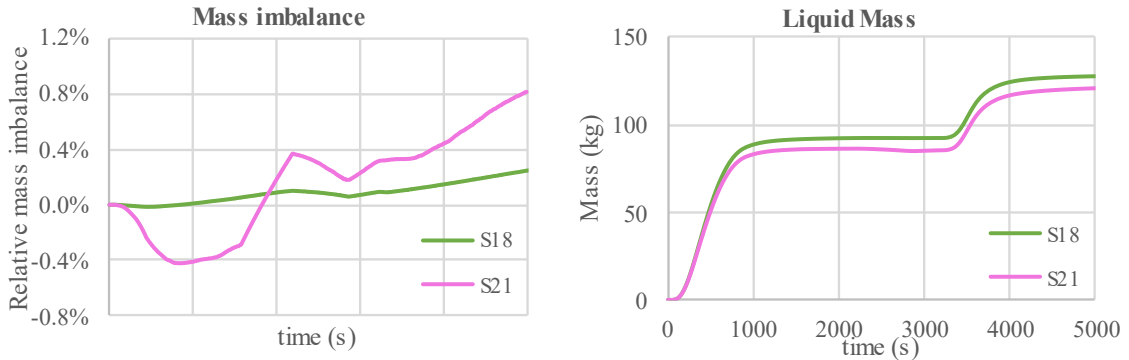


**Figure 48 – Mass imbalance and liquid mass from S18 and S21**

It was observed that the utilization of larger residuals (S21) barely affected the temperature transient (+0.1%), but provided lower liquid mass (-6.3%) by the end of the interval analyzed, even though the condensation rate did not change, as it can be seen in Figure 46. The utilization of lower residuals increased the computational effort required by the simulation (an increase of 173% was verified in the number of iterations required per time step), but it improved the total mass imbalance that could be reduced from 0.81% to 0.25%. For this reason, the residuals used for S18 ( $10^{-5}/10^{-7}$ ) were used for all the simulations performed along this thesis.

### 5.7.3. Condensation/evaporation relaxation coefficients

Simulations S18, S22, and S23 were performed to verify the influence of the condensation relaxation coefficients used to model bulk steam condensation and liquid evaporation. Figures 49, 50, and 51 present the results obtained by the numerical analysis with regard to the influence of the phase change relaxation coefficients:

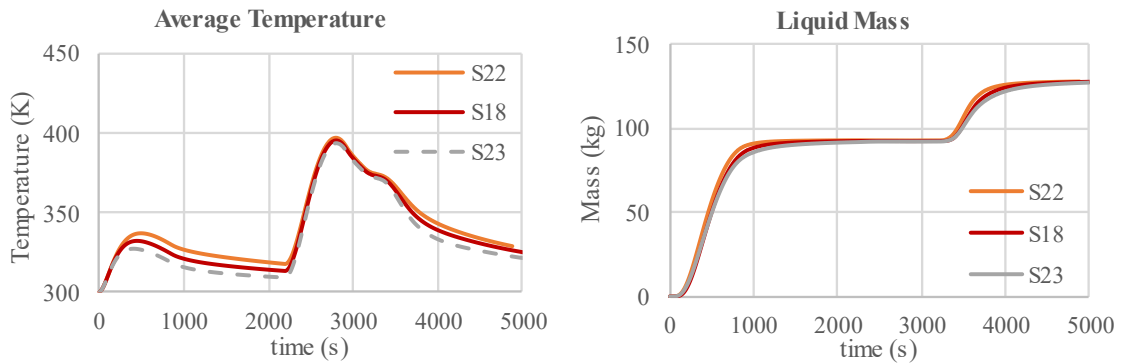


Figure 49 – Temperature and liquid mass transient from S18, S22, and S23

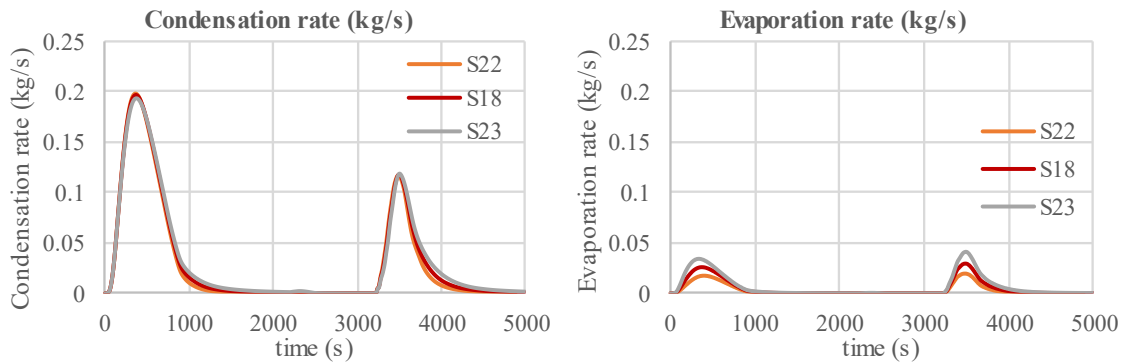
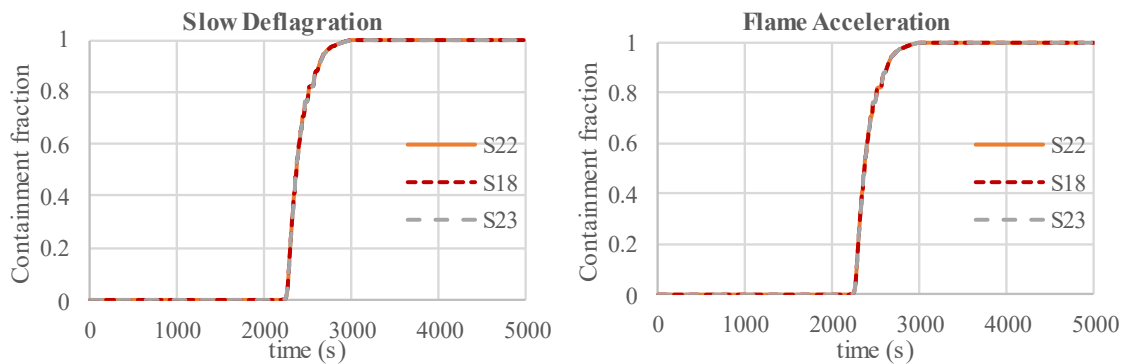


Figure 50 – Condensation and evaporation mass rates from S18, S22, and S23



**Figure 51 – Fraction of the containment under SD and FA risk from S18, S22, S23**

It was observed that the utilization of coefficients 50% lower and 100% higher than the provided by the empirical Lee Model did not affect significantly the fraction of the containment under SD and FA risks. It was observed differences on the evaporation mass rates for different relaxation coefficients. The maximum evaporation rates ranged from 0.02 to 0.04 kg/s. No significant difference was observed for the condensation rates, it occurs mostly on the walls, and the relaxation coefficients are employed in the modeling of bulk evaporation and condensation.

## **5.8. Accident progression**

The description of the progression of the accident presented in this Section is based on the results provided by Simulation S6, and are organized according to the main phases observed: steam release, hydrogen release and hydrogen stratification.

### **5.8.1. Steam release**

During the first release of steam in the containment, it was observed increase of the average temperature, accumulation of steam in the top part of the containment, and wall condensation, as presented in Figure 52. The maximum temperature reached during this phase is 331.9 K at 455 s.

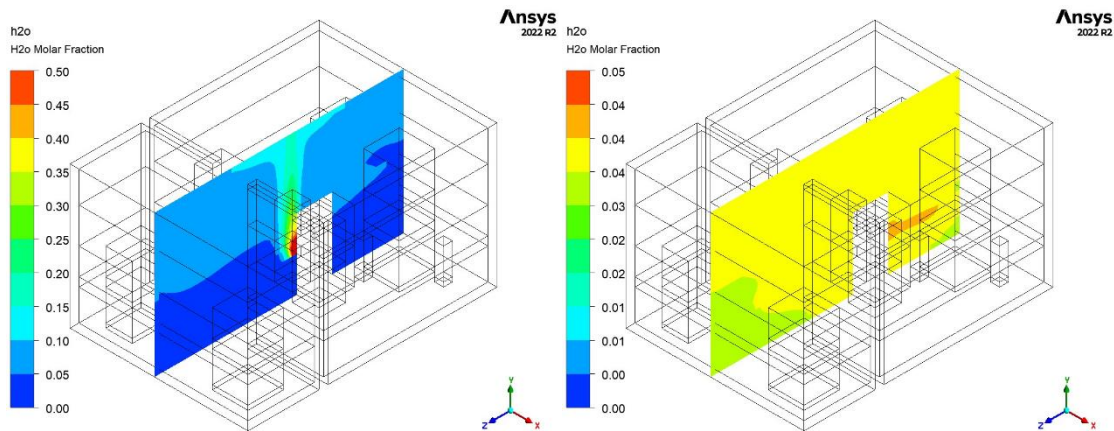


**Figure 52 –Steam mole fraction in the break longitudinal plane at 340 and 1500 sec**

The steam release ends at 867 s, and a reduction in the average temperature is observed until the beginning of the release of hydrogen. The concentration of steam in the containment also decreases, as it condenses on the walls, and becomes nearly constant at 3% from 1000s to 2000s and homogeneous over all the containment.

### **5.8.2. Hydrogen release**

Hydrogen is released from 2193 s and ends at 2926 s. A significant increase in the temperature is observed during this phase, since this gas only exchanges heat with the containment walls by natural convection. The containment maximum average temperature reached during the accident is 410 K (S6) and occurs at 2810 s. Figure 53 illustrates the temperature and hydrogen mole fraction distribution in the break longitudinal section at this instant:

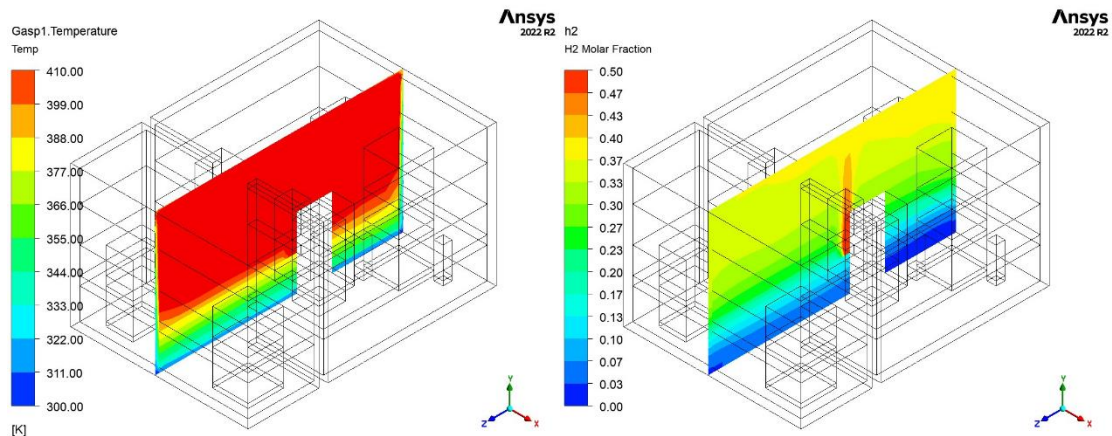


**Figure 53 –Temperature and hydrogen profile at cabin longitudinal section, 2810 sec**

During this phase, the containment undergoes the possibility of combustion through the regimes of SD, FA and DDT. Table 18 summarizes the main parameters that drive the SD and FA risk, and the fraction of the containment under the risk of these combustion regimes during the phase of hydrogen release.

**Table 18 : Fractions of the containment under SD and FA risk (S6)**

<b>Time (s)</b>	<b>Fraction under SD risk</b>	<b>Fraction under FA risk</b>	<b>H<sub>2</sub> average mole fraction</b>	<b>Average Temperature (K)</b>
2300	25%	0.3%	2.2%	322.1
2370	50%	21.1%	5.4%	336.9
2506	75%	60.6%	13.4%	370.0
3058	100%	86.2%	27.8%	393.3

Figures 54, 55, 56, and 57 illustrate the containment cells under risk of SD and FA for the instants presented in Table 18. The increase of hydrogen concentration and temperature triggers the criterion for possibility of SD and FA in the containment.

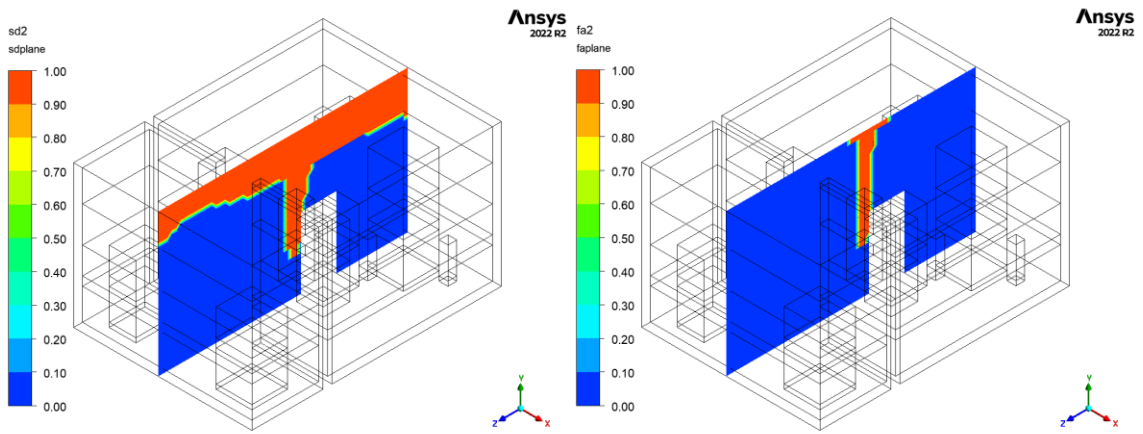


**Figure 54 –Containment zones under SD and FA risk at 2300 sec**

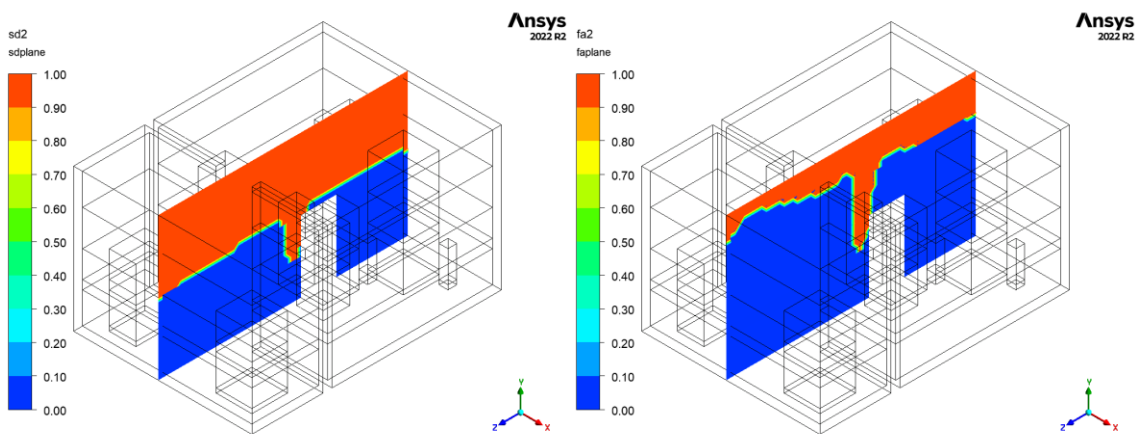


**Figure 55 –Containment zones under SD and FA risk at 2370 sec**

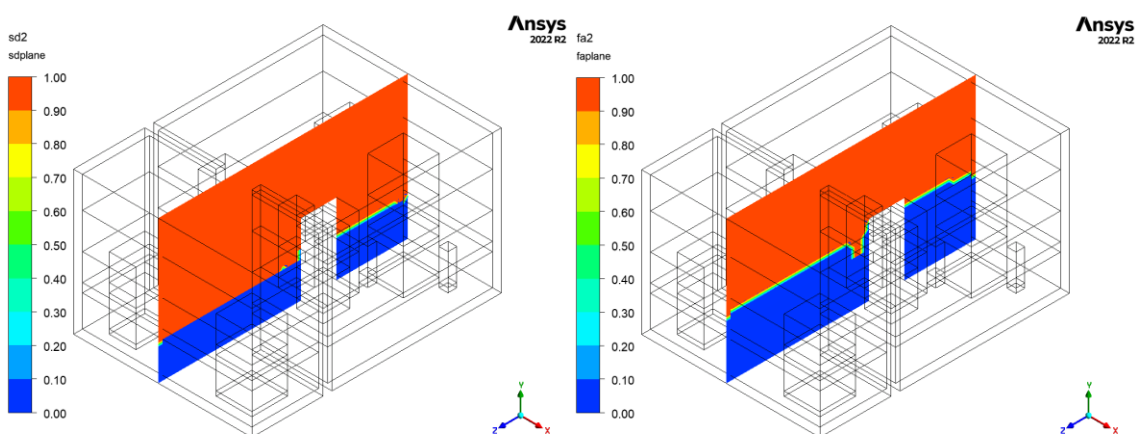


**Figure 56 –Containment zones under SD risk at 2505 sec**

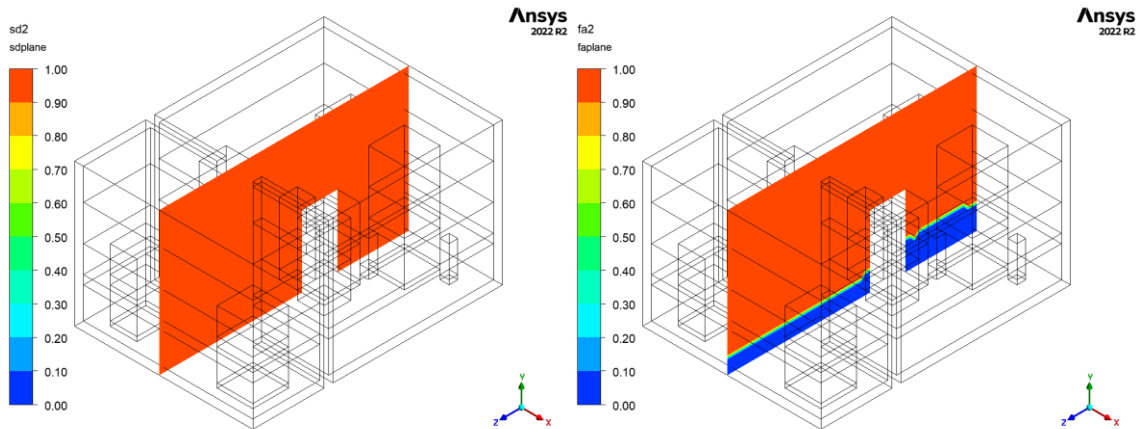


**Figure 57 – Containment zones under SD risk at 3060 sec**

Figure 58 illustrates the transient of average hydrogen mole fraction and containment temperature during the accident:

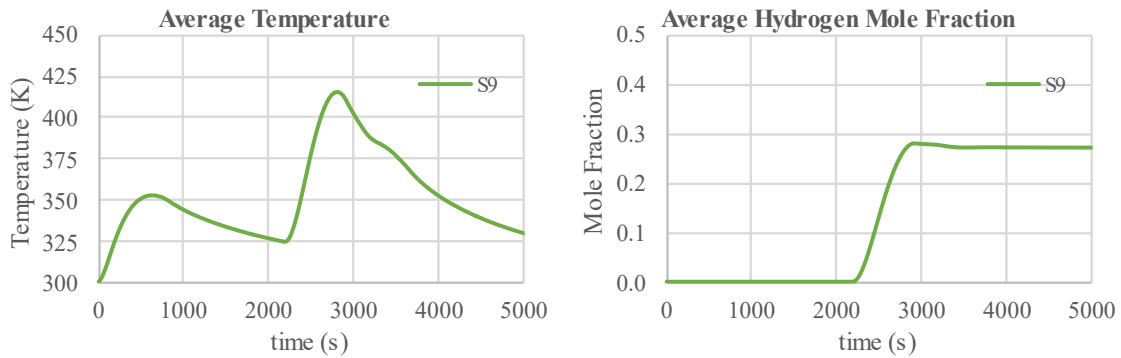


**Figure 58 – Average temperature and hydrogen mole fraction transient**

### 5.8.3. Hydrogen stratification

After the hydrogen release, a stratified layer rich of the gas is verified on the top of the containment. The hydrogen cloud is formed in both containment rooms and reaches hydrogen mole fraction higher than 35%, and steam mole fractions about 2%, as presented in Figure 59.

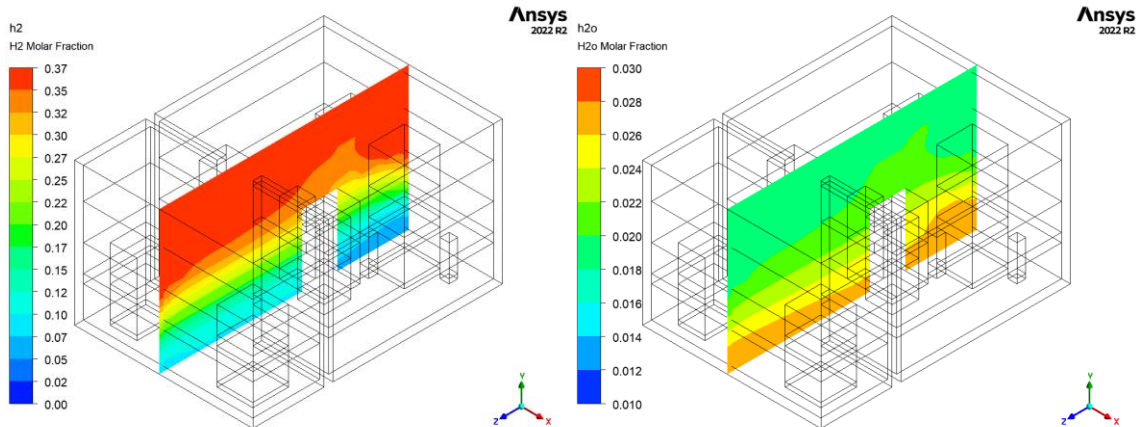


**Figure 59 – Hydrogen and steam mole fraction on the longitudinal plane at 3100 sec**

This verified stratification of the hydrogen is momentarily affected by the steam released between 3123 and 3659 seconds, but returns after the end of the release and is smoothed by the uniformization of temperature inside the containment, as presented in Figure 60. After 5000 s, the hydrogen concentration on the top of the containment is about 30%, while the concentration in the bottom is about 19%. Any of the hydrogen concentrations verified at 5000 s are enough to support DDT.

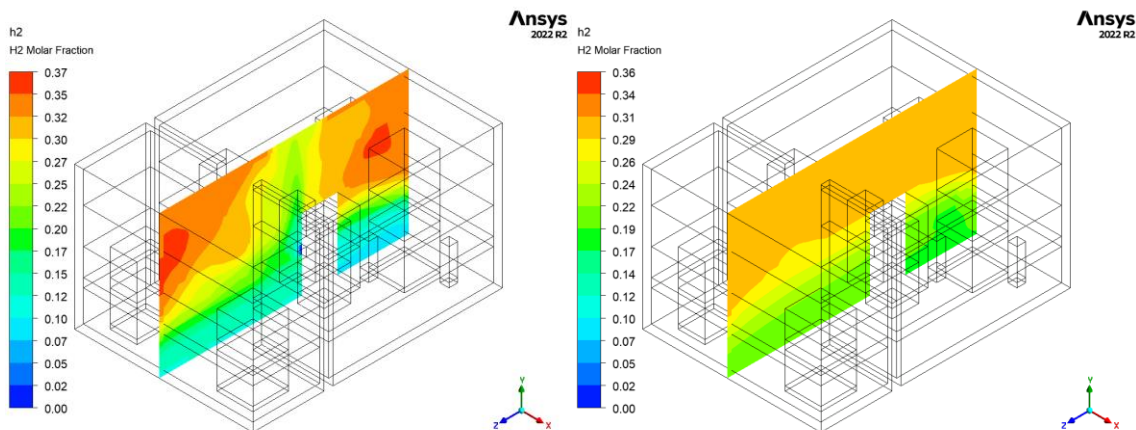


**Figure 60 – Hydrogen mole fraction on the longitudinal plane at 3400 and 5000 sec**

## 6. CONCLUSION

Simulating the progression of an accident in a nuclear reactor containment is a complex task and requires large computational processing capabilities, since the geometry involved, and the transient analyzed are typically very large. Moreover, the presence of different phases and species in the model increase the number of equations solved by the code, and the occurrence of complex phenomena such as steam condensation in the presence of non-condensable gases require additional models for the simulation.

The improvements verified for the computational capabilities over the last decades have made feasible the utilization of CFD codes to perform three-dimensional containment analysis. Several studies focused on hydrogen risk assessment in nuclear reactor containments were published and are available in academic literature. Most of them neglect the steam condensation expected to occur during an accident with boiling of the primary coolant in the core of the reactor and further condensation on the walls of the containment. This simplification is a result of the limitations of computational capacity, but mostly due to the absence of in-built condensation models in commercial CFD codes.

The simulations performed during this thesis showed that their results are independent of the mesh selected for the simulation, as it was verified by the grid convergence analysis. A mesh composed of about 62,000 hexahedral elements of 25 cm of size provided a discretization uncertainty of about 3% and allowed running simulations with reasonable and achievable computational effort. Furthermore, the numerical analysis

verified that the utilization of different under-relaxation factors for the externally implemented condensation mass source term did not affect the results obtained.

The absence of experimental data for validation of the simulations results required the development of a zero-dimensional theoretical model based on the conservation equations of mass and energy, which could be used to predict average temperatures and pressures expected for the simulations in the long-term after the thermal equilibrium is reached in the containment.

The results obtained by the simulations with different empirical models for condensation in the presence of non-condensable gases and different bulk condensation and evaporation conditions showed that even though condensation plays an important role in removing heat from the containment, it can also reduce the concentration of steam in the interior of the containment, what is responsible to increase the concentrations of air and hydrogen in the flammable gas mixture and increases the possibility of combustion. Nevertheless, these factors were shown to be less relevant for the achievement of combustion criteria than the hydrogen concentration. No significant difference was verified between the several scenarios analyzed with regard to the combustion regime likelihood. This conclusion may have been obtained because a very significant amount of hydrogen was released, resulting in the likelihood of combustion exclusively due to the large hydrogen concentrations.

It was verified that the empirical condensation correlation proposed by Tagami provided slower condensation on the containment walls, compared to Dehbi's and

Uchida's, what was responsible by more slowly heat removal from the containment and higher average temperatures in the beginning of the transient.

Furthermore, no significant difference was verified for the horizontal positioning of the break in the primary circuit, since the release of steam and hydrogen is expected ascend in the containment and reach the ceiling wall before reaching the vertical walls. Initially, hydrogen stratification is observed in the top of the containment, but as the accident progresses and the differences of temperature over the containment decrease, there is not much temperature difference anymore resulting in large densities differences to support the stratification. At this point, the hydrogen distribution over all the volume becomes more uniform and all the containment becomes under combustion risk.

Finally, the developed methodology seemed to be feasible to also model the response of the hydrogen mitigation system composed by passive autocatalytic recombiners during the progression of an accident. The chemical reaction of recombination of hydrogen and oxygen can be suitably modeled using a similar approach to the one adopted to model the condensation phenomena. Mass sinks for the hydrogen and oxygen species can be implemented, and sources of energy and steam are also introduced, if a condition regarding the required concentrations and activation energy of the reaction is met.

## REFERENCES

- [1] “Nuclear Energy for a Net Zero World,” *INTERNATIONAL ATOMIC ENERGY AGENCY*. IAEA, Vienna, 2021.
- [2] M. Sethi, *The Global Nuclear Landscape*, 1st ed. London: Routledge, 2023. doi: 10.4324/9781003400196.
- [3] M. M. Rahman, J. Dongxu, N. Jahan, M. Salvatores, and J. Zhao, “Design concepts of supercritical water-cooled reactor (SCWR) and nuclear marine vessel: A review,” *Progress in Nuclear Energy*, vol. 124, p. 103320, Jun. 2020, doi: 10.1016/J.PNUCENE.2020.103320.
- [4] U.S. Atomic Energy Commission, “General Design Criteria for Nuclear Power Plants, Code of Federal Register, 10 CFR 50 Appendix A,” 1971.
- [5] B. R. Sehgal, “Light Water Reactor Safety: A Historical Review,” *Nuclear Safety in Light Water Reactors*, pp. 1–88, Jan. 2012, doi: 10.1016/B978-0-12-388446-6.00001-0.
- [6] M. Leyse, *Preventing Hydrogen Explosions In Severe Nuclear Accidents: Unresolved Safety Issues Involving Hydrogen Generation And Mitigation*. New York, 2014.
- [7] D. W. Stamps and M. Berman, “High-Temperature Hydrogen Combustion in Reactor Safety Applications,” *Nuclear Science and Engineering*, vol. 109, no. 1, pp. 39–48, 1991, doi: 10.13182/NSE91-A23843.

- [8] J. M. Martín-Valdepeñas, M. A. Jiménez, F. Martín-Fuertes, and J. A. Fernández, “Improvements in a CFD code for analysis of hydrogen behaviour within containments,” *Nuclear Engineering and Design*, vol. 237, no. 6, pp. 627–647, Mar. 2007, doi: 10.1016/J.NUCENGDES.2006.09.002.
- [9] D. M. Prabhudharwadkar, K. N. Iyer, N. Mohan, S. S. Bajaj, and S. G. Markandeya, “Simulation of hydrogen distribution in an Indian Nuclear Reactor Containment,” *Nuclear Engineering and Design*, vol. 241, no. 3, pp. 832–842, Mar. 2011, doi: 10.1016/J.NUCENGDES.2010.11.012.
- [10] D. C. Visser, M. Houkema, N. B. Siccama, and E. M. J. Komen, “Validation of a FLUENT CFD model for hydrogen distribution in a containment,” *Nuclear Engineering and Design*, vol. 245, pp. 161–171, Apr. 2012, doi: 10.1016/J.NUCENGDES.2012.01.025.
- [11] R. K. Raman, K. N. Iyer, R. S. Rao, A. J. Gaikwad, and S. K. Sharma, “CFD studies of hydrogen distribution in 220 MWe PHWR containment,” *Nuclear Engineering and Design*, vol. 396, p. 111898, Sep. 2022, doi: 10.1016/J.NUCENGDES.2022.111898.
- [12] R. Gharari, H. Kazeminejad, N. M. Kojouri, and A. Hedayat, “Analysis of the gases distribution during a severe accident by coupling the MELCOR and FLUENT in WWER1000 containment,” *Process Safety and Environmental Protection*, vol. 162, pp. 97–111, Jun. 2022, doi: 10.1016/J.PSEP.2022.04.008.

- [13] H. Zhao, X. Luo, R. Zhang, X. Lyu, H. Yin, and Z. Kang, “Analysis on hydrogen risk under LOCA in marine nuclear reactor,” *Exp Comput Multiph Flow*, vol. 4, Apr. 2021, doi: 10.1007/s42757-020-0077-2.
- [14] X. Lyu, S. Liu, K. Ji, Y. Feng, S. Wang, and Z. Huang, “Research on hydrogen risk and hydrogen control system in marine nuclear reactor,” *Ann Nucl Energy*, vol. 141, p. 107373, Jun. 2020, doi: 10.1016/J.ANUCENE.2020.107373.
- [15] F. P. Incropera, *Fundamentals of heat and mass transfer : Frank P. Incropera ... [et al.]*, 6th ed. Hoboken, N.J: Wiley, 2007.
- [16] D. Labuntsov, “Heat transfer in film condensation of pure steam on vertical surfaces and horizontal tubes (in Russian),” *Heat Power Eng*, vol. 4, no. 7, pp. 72–79, 1957.
- [17] J. C. de la Rosa, A. Escrivá, L. E. Herranz, T. Cicero, and J. L. Muñoz-Cobo, “Review on condensation on the containment structures,” *Progress in Nuclear Energy*, vol. 51, no. 1, pp. 32–66, Jan. 2009, doi: 10.1016/J.PNUCENE.2008.01.003.
- [18] W. J. Minkowycz and E. M. Sparrow, “Condensation heat transfer in the presence of noncondensables, interfacial resistance, superheating, variable properties, and diffusion,” *Int J Heat Mass Transf*, vol. 9, no. 10, pp. 1125–1144, Oct. 1966, doi: 10.1016/0017-9310(66)90035-4.
- [19] A. Dehbi, “The effects of noncondensable gases on steam condensation under turbulent natural convection conditions,” 1991.

- [20] Q. Wu and M. Corradini, "Integral Reactor Containment Condensation Model and Experimental Validation," Idaho Falls, ID (United States), May 2016. doi: 10.2172/1258470.
- [21] T. Wang, D. Wang, L. Tong, and X. Cao, "Improvement of Condensation Model With the Presence of Non-Condensable Gas for Thermal-Hydraulic Analysis in Containment," *Front Energy Res*, vol. 9, 2021, doi: 10.3389/fenrg.2021.671539.
- [22] H. Uchida, A. Oyama, and Y. Togo, "EVALUATION OF POST-INCIDENT COOLING SYSTEMS OF LIGHT WATER POWER REACTORS," Country unknown/Code not available, 1964. [Online]. Available: <https://www.osti.gov/biblio/4023463>
- [23] T. Tagami, "Interim report on safety assessments and facilities establishment project for June 1965, No. 1," *Japanese Atomic Energy Research Agency*, 1965.
- [24] A. Dehbi, M.W. Golay, and M.S. Kazimi, "Condensation experiments in steam–air and steam–air–helium mixtures under turbulent natural convection," *National Heat Transfer Conf.*, pp. 19–28, 1991.
- [25] A. Dehbi, "A generalized correlation for steam condensation rates in the presence of air under turbulent free convection," *Int J Heat Mass Transf*, vol. 86, pp. 1–15, Jul. 2015, doi: 10.1016/J.IJHEATMASSTRANSFER.2015.02.034.
- [26] Y. Kataoka, T. Fukui, S. Hatamiya, T. Nakao, M. Naitoh, and I. Sumida, "Experiments on Convection Heat Transfer Along a Vertical Flat Plate Between Pools with Different Temperatures," *Nucl Technol*, vol. 99, no. 3, pp. 386–396, 1992, doi: 10.13182/NT92-A34722.

- [27] C. Allison, “Phenomenology of Severe Accident,” *IAEA sponsored training workshops on Analysis of Severe Accident*.
- [28] Borgnakke C, Sonntag RE, and Van Wylen GJ, *Fundamentals of Thermodynamics*, 7th ed. Hoboken NJ: Wiley, 2009.
- [29] K. T. Møller, T. R. Jensen, E. Akiba, and H. wen Li, “Hydrogen - A sustainable energy carrier,” *Progress in Natural Science: Materials International*, vol. 27, no. 1, pp. 34–40, Feb. 2017, doi: 10.1016/J.PNSC.2016.12.014.
- [30] Z. M. Shapiro and T. R. Moffette, “Hydrogen Flammability Data And Application To Pwr Loss-Of-Coolant Accident,” 1957.
- [31] M. Fernandez-Cosials, “ANALYSIS AND IMPROVEMENT OF HYDROGEN MITIGATION STRATEGIES DURING A SEVERE ACCIDENT IN NUCLEAR CONTAINMENTS,” 2017. doi: 10.20868/UPM.thesis.47657.
- [32] OECD/NEA, *Flame Acceleration and Deflagration-to-Detonation Transition in Nuclear Safety*. Paris: NEA/CSNI/R, 2000.
- [33] C. S. Byun, D. W. Jerng, N. E. Todreas, and M. J. Driscoll, “Conceptual design and analysis of a semi-passive containment cooling system for a large concrete containment,” *Nuclear Engineering and Design*, vol. 199, no. 3, pp. 227–242, Jul. 2000, doi: 10.1016/S0029-5493(00)00228-4.
- [34] R. K. C. J. Kumar, “Flammability Limits of Hydrogen-Oxygen-Diluent Mixtures,” *J Fire Sci*, vol. 3, pp. 245–262, 1985.

- [35] J. M. Martín-Valdepeñas Yagüe, “Modelos numéricos acoplados a un código fluidodinámico para el análisis del riesgo de combustión de hidrógeno en contenciones,” Jun. 2004. doi: 10.20868/UPM.thesis.429.
- [36] S. B. Dorofeev, M. S. Kuznetsov, V. I. Alekseev, A. A. Efimenko, and W. Breitung, “Evaluation of limits for effective flame acceleration in hydrogen mixtures,” *J Loss Prev Process Ind*, vol. 14, no. 6, pp. 583–589, Nov. 2001, doi: 10.1016/S0950-4230(01)00050-X.
- [37] S. B. Dorofeev, A. A. Efimenko, and A. V. Besmel'nitsyn, “DDT Scaling for Severe Accidents. Detonation Cell Size Data as a Function of Composition and Initial Conditions,” 1997.
- [38] S. R. Ravva, K. N. Iyer, S. K. Gupta, and A. J. Gaikwad, “Implementation and validation of the condensation model for containment hydrogen distribution studies,” *Nuclear Engineering and Design*, vol. 270, pp. 34–47, Apr. 2014, doi: 10.1016/J.NUCENGDES.2013.12.047.
- [39] ANSYS Inc, “Ansys Fluent Theory Guide,” no. 2022 R2. Canonsburg, 2022.
- [40] W. Lee, “A Pressure Iteration Scheme for Two-Phase Flow Modeling,” *Computational Methods for Two-Phase Flow and Particle Transport*. WORLD SCIENTIFIC, May 1979.
- [41] J. De Li, “CFD simulation of water vapour condensation in the presence of non-condensable gas in vertical cylindrical condensers,” *Int J Heat Mass Transf*, vol. 57, no. 2, pp. 708–721, Feb. 2013, doi: 10.1016/J.IJHEATMASSTRANSFER.2012.10.051.

- [42] American Society of Mechanical Engineers, “Standard for verification and validation in computational fluid dynamics and heat transfer - V&V20,” 2009.
- [43] V. Gaioni and M. Fernandez-Cosials, “A Practical Verification and Validation Procedure for Computational Fluid Dynamics,” 2020. doi: 10.13140/RG.2.2.15073.33121.